Exciton States in Monolayer $MoSe_2$ and $MoTe_2$ Probed by Upconversion Spectroscopy

B. Han,[1] C. Robert,[1] E. Courtade,[1] M. Manca,[1] S. Shree,[1] T. Amand,[1] P. Renucci,[1] T. Taniguchi,[2] K. Watanabe,[2] X. Marie,[1] L. E. Golub,[3] M. M. Glazov,[3,*] and B. Urbaszek[1,†]

[1]*Université de Toulouse, INSA-CNRS-UPS, LPCNO, 135 Avenue Rangueil, 31077 Toulouse, France*
[2]*National Institute for Materials Science, Tsukuba, Ibaraki 305-0044, Japan*
[3]*Ioffe Institute, 194021 St. Petersburg, Russia*

(Received 11 May 2018; revised manuscript received 16 July 2018; published 18 September 2018)

Transitions metal dichalcogenides (TMDs) are direct gap semiconductors in the monolayer (ML) limit with fascinating optical and spin-valley properties. The strong optical absorption of up to 20% for a single ML is governed by excitons, electron-hole pairs bound by Coulomb attraction. Excited exciton states in $MoSe_2$ and $MoTe_2$ monolayers have so far been elusive because of their low oscillator strength and strong inhomogeneous broadening. Here, we show that encapsulation in hexagonal boron nitride results in an emission line width of the A:1*s* exciton below 1.5 meV and 3 meV in our $MoSe_2$ and $MoTe_2$ monolayer samples, respectively. This allows us to investigate the excited exciton states by photoluminescence upconversion spectroscopy for both monolayer materials. The excitation laser is tuned into resonance with the A:1*s* transition, and we observe emission of excited exciton states up to 200 meV above the laser energy. We demonstrate bias control of the efficiency of this nonlinear optical process. We discuss the origin of the upconversion effect. Our model calculations suggest an exciton-exciton (Auger) scattering mechanism specific to TMD MLs involving an excited conduction band, thus generating high-energy excitons with small wave vectors. The optical transitions are further investigated by white light reflectivity, photoluminescence excitation, and resonant Raman scattering, confirming their origin as excited excitonic states in monolayer thin semiconductors.

DOI: 10.1103/PhysRevX.8.031073 Subject Areas: Optoelectronics, Semiconductor Physics

I. INTRODUCTION

Transition metal dichalcogenides such as MoS_2, WS_2, WSe_2, $MoSe_2$, and $MoTe_2$ are direct band-gap semiconductors when thinned down to one monolayer [1–6]. Their band gap is situated in the visible to near infrared of the optical spectrum. Since the Coulomb interaction is strong in this ultimate two-dimensional (2D) limit, the optical properties are dominated by excitons—bound electron-hole pairs [7–14]. Recently, encapsulation in hexagonal boron nitride (hBN) of TMD monolayers (MLs) has resulted in considerable narrowing of the exciton transition linewidth down to 1 meV [15–24]. This result gives us access to fine features of the exciton spectra that dominate the linear and nonlinear optical properties of monolayer semiconductors.

Optical excitation of a semiconductor at the band gap typically results in luminescence at lower energy due to energy relaxation of charge carriers and excitons. In Figs. 1(a)–1(d), we show that resonant laser excitation of the lowest-energy exciton resonance A:1*s* results in pronounced photoluminescence (PL) emission at *higher* energy than the excitation laser for four different TMD ML materials. This effect is generally termed upconversion and has been observed for different semiconductor structures such as InP/InAs heterojunctions, CdTe quantum wells, and InAs quantum dots [25–29], albeit based on different microscopic mechanisms. Upconversion has previously been reported for WSe_2 [16,30] and MoS_2 [31] MLs. These experiments allow detailed insight into the light-matter interaction physics of excitons in TMD monolayers: First, clarifying the origin of the upconversion signal is in itself a crucial problem, as the origin of excess energy needs to be identified and the role of exciton-exciton scattering mechanisms is revealed. Second, upconversion spectroscopy gives us access to the excited exciton states that govern absorption and emission, which are so far not well understood in ML $MoSe_2$ and $MoTe_2$. The relative motion of the electron and hole in the exciton, in analogy to the hydrogen atom and positronium, is characterized by a principle quantum number $n = 1, 2, 3\ldots$, where typical photoluminescence emission stems from the $n = 1$ exciton of the A-exciton series, labeled A:1*s*. The optical absorption in energy above the A:1*s*

*glazov@coherent.ioffe.ru
†urbaszek@insa-toulouse.fr

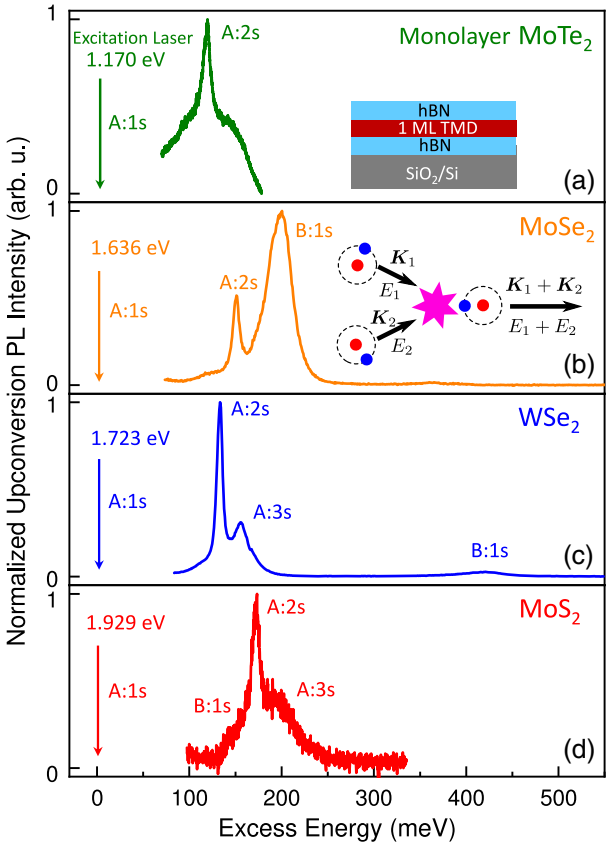

FIG. 1. Upconversion spectroscopy in TMD monolayers. We present, for four different monolayer materials, resonant excitation experiments of the A:1s exciton at $T = 4$ K, which result in PL emission at higher energy. The laser energy—equal to the A:1s transition energy—is marked by a vertical arrow. The upconversion emission peaks are labeled A:2s and B:1s, where the origin of these peaks is confirmed in complementary experiments such as reflectivity and PLE. The results for WSe_2 are reproduced from Ref. [16], and the MoS_2 results from Ref. [31]. The inset in panel (a) shows a scheme of the sample. The inset in panel (b) shows the exciton-exciton Auger process, where one exciton annihilates and another one acquires total momentum and energy of the two particles.

optical transition will be determined by the excited states A:2s, 3s, etc. and the B-exciton series, separated from the A-exciton mainly by the spin-orbit splitting in the 200–400-meV range [32]. Upconversion allows us to access excited exciton states for $MoSe_2$ and $MoTe_2$, which is not possible in samples that are not encapsulated in hBN as the excited A-excitons spectrally overlap with the B-exciton series. We demonstrate bias control of the upconversion process. We provide an in-depth study of exciton states in $MoTe_2$, comparing upconversion with photoluminescence excitation spectroscopy (PLE) and white light reflectivity. In the last part of the paper, we provide a theoretical model and discuss the origin of upconversion in TMD monolayers. Our model calculations suggest that Auger-type exciton-exciton scattering could be very efficient in TMD MLs as compared to other semiconductor nanostructures due to (i) the strong Coulomb interaction, which makes it possible to relax the single-electron momentum conservation [33,34], and (ii) the possibility of a resonant processes involving exciton transfer to an excited energy band.

II. EXCITED-STATE SPECTROSCOPY IN ML $MoSe_2$

Monolayer $MoSe_2$ is a very versatile TMD material ideally suited to explore coupling to optical cavities [35,36], investigating voltage control of monolayer mirrors [37,38], and the interplay between charged and neutral excitons [39]. Most of these experiments are based on the optical response of the lowest-energy exciton state A:1s, but very little is known about excited exciton states that govern optical absorption at higher energies and energy relaxation pathways for PL emission.

The experimental results for the high-quality $MoSe_2$ samples encapsulated in hBN [40] are summarized in Fig. 2; details of the experimental setup can be found in Appendix A. In differential white light reflectivity at $T = 4$ K, we clearly observe the A- and B-exciton 1s states [41–43], the A:1s resonance has a full width at half maximum (FWHM) of the order of 2 meV [44]. In Fig. 2(a), we show an intriguing result: Excitation of the sample with a low-power, continuous-wave (cw), narrow-linewidth (<1 μeV) laser at the A:1s energy results in emission of the B:1s transition at *higher* energy. As we scan the laser across the A:1s resonance, the PL intensity (black graph) has a clear maximum in intensity when the laser is exactly at the A:1s resonance; the blue data points represent the integrated upconversion intensity for different laser energies. In addition to B:1s, another transition appears about 150 meV above the A:1s in upconversion PL, which we tentatively assign to the excited A-exciton A:2s state. This transition is also visible in reflectivity in Fig. 2(b). For samples directly exfoliated onto SiO_2, the excited A-exciton states were not directly accessible due to their overlap with the B-exciton 1s state. A fingerprint of the A:2p state was reported in two-photon PLE experiments [43], where the B:1s state absorption is strongly reduced [45].

Now, we investigate the origin of the upconversion PL in ML $MoSe_2$ shown in Figs. 1(b) and 2(a). We compare the evolution of standard and upconversion PL intensity as a function of laser power in Fig. 2(c). The slope of the upconversion intensity versus laser power (1.64) integrated over the combined A:2s and B:1s emission is roughly twice as high as for standard PL (0.88), consistent with a two-photon (two-exciton) process being at the origin of this nonlinear optical effect. We note that the exact power dependence determination for upconversion PL depends slightly on the spectral range used for signal integration. For example, the slope for a narrow spectral range at the A:2s (B:1s) resonance is

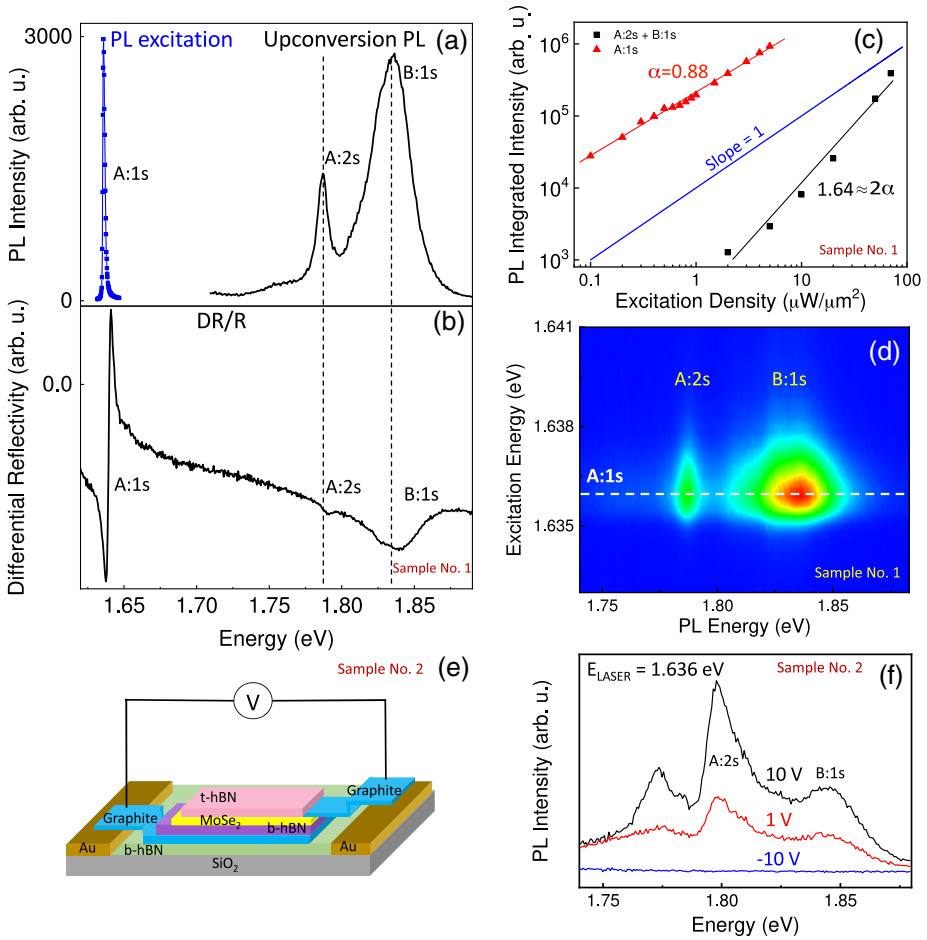

FIG. 2. Control of upconversion in ML $MoSe_2$ for $T = 4$ K. Sample No. 1: (a) Scanning a Ti-Sa laser across the A:1s transition, which results in upconversion emission of the A:2s and B:1s transitions (black curve for excitation exactly at resonance). Blue symbols give the integrated upconversion intensity as a function of laser energy. (b) Reflection contrast for the same sample spot, confirming the energy positions of A:1s, A:2s, and B:1s transitions. (c) The power dependence of the upconversion signal shows an increase with a slope of roughly 1.64 (black symbols), as compared to the standard A:1s exciton emission with a slope of roughly half (0.88—red symbols) using a HeNe laser for excitation. (d) Contour plot (blue—below 50 counts; red—greater than 2000 counts) of upconversion PL intensity as the excitation laser is swept across the A:1s resonance. Sample No. 2: (e) Schematics of the charge tunable device. (f) Voltage control of upconversion. The signal is maximal in the neutral regime and gets weaker as the n-type regime favors trion and not neutral exciton absorption; the B:1s and A:2s emission are marked; a third emission peak of yet-to-be-determined origin appears at lower energy.

roughly 2 (1.8). In Fig. 2(d), we plot the upconversion emission as the laser is scanned across the A:1s resonance. Upconversion is only detectable over a 2-meV range of laser energy when the laser is in resonance with the A:1s state. This indicates that upconversion is a resonant process, as observed for WSe_2 monolayers [16]. This conclusion gets additional support from upconversion experiments in a charge tunable device [Fig. 2(e)], presented in Fig. 2(f). At a bias of +10 V, the excitation laser is tuned into resonance with the neutral A:1s state. As the applied voltage is lowered to +1 V, electrons are added to the monolayer, decreasing absorption strength at the neutral exciton resonance. The upconversion signal is not detectable anymore for a bias of −10 V, as absorption at the exciton resonance is inefficient; this is because the charged exciton absorption, at a different energy, dominates [37,38,41]. Differential reflectivity of our device shows a strong neutral exciton resonance at +10 V, whereas for −10 V, the charged exciton transition dominates; see reflectivity measurements on the device in Appendix B. These experiments confirm that upconversion PL emission has its origin in resonant neutral exciton generation and can be controlled electrically in charge tunable structures. Note that for a quantitative analysis of the bias tuning of the upconversion efficiency, the slight shift of the central A:1s transition energy (neutral exciton) with bias also needs to be taken into account. However, in our sample, this shift in energy for the A:1s regime is considerably smaller than the transition linewidth.

III. EXCITED-STATE SPECTROSCOPY IN ML $MoTe_2$

$MoTe_2$ is a very interesting layered material [46–48], which provides the fascinating opportunity to switch between semiconducting $2H$ and metallic phases by tuning strain or carrier concentration [49,50]. This material allows us to work towards devices based on bias-controlled phase changes in monolayer $MoTe_2$ [51,52]. The first studies of $2H - MoTe_2$ flakes exfoliated on SiO_2 have identified monolayers as direct band gap semiconductors [53,54]; interestingly, the nature of the gap of the bilayer is still under discussion [55,56]. So, in practice, the monolayers have to be distinguished from bilayers in Raman scattering experiments; see Fig. 7a. $MoTe_2$ MLs have an optical band gap at $T = 4$ K at 1.17 eV, corresponding to an emission wavelength of 1050 nm. Therefore, its alloying with other TMD materials, such as MoS_2 and $MoSe_2$, allows one, in principle, to cover the full spectral range from 630 to 1050 nm for optoelectronics applications. As optical absorption is not only strong at the excitonic band gap (A:1s) but also for higher-lying exciton states [7–14], better knowledge of the excited exciton spectrum is needed. This knowledge also allows us, in principle, to get an estimation of the exciton binding energy by comparing the data with model calculations of exciton states in a screened 2D potential [10,31,57,58].

Here, we show the striking impact of hBN encapsulation on the optical properties of monolayer $MoTe_2$. The PL spectrum in Fig. 3(b) shows very narrow emission lines (FWHM linewidth of 3 meV) for the neutral exciton at the A:1s state at 1.17 eV, approaching the optical quality reported for hBN encapsulated MoS_2 and WSe_2 monolayers [15–21]. We confirm the high sample quality in reflectivity experiments in Fig. 3(a), which show this transition basically at the same energy as in PL, indicating negligible neutral exciton localization. In reflectivity, we also see a broader transition about 250 meV above the A:1s, which we ascribe to the B:1s state, following comparison with the data from the literature [53,54,59]. We also observe in reflectivity a transition 120 meV above the A:1s state, not reported previously, which we ascribe to the A:2s state. Strikingly, when exciting with a laser

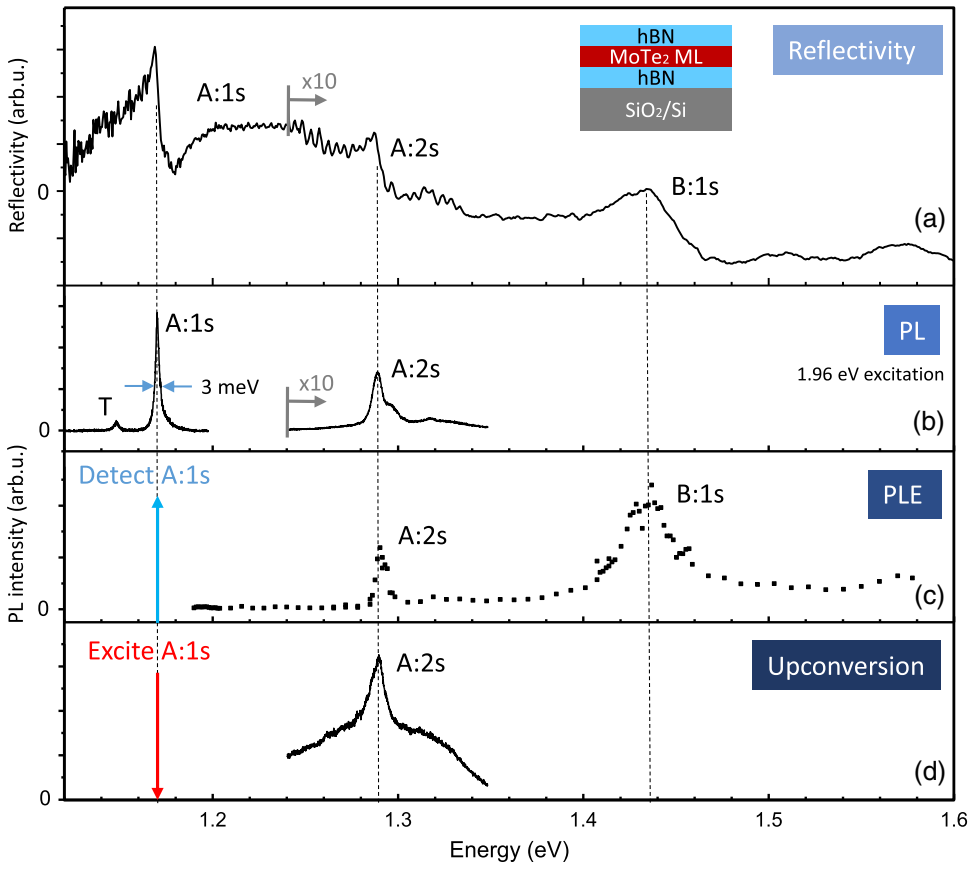

FIG. 3. Exciton spectroscopy in $MoTe_2$ monolayers encapsulated in hBN for $T = 4$ K. (a) Differential reflectivity spectrum. The energy positions of the exciton transitions A:1s, A:2s, and B:1s are marked. (b) Excitation with a HeNe laser at 1.96 eV, resulting in hot PL of the A:2s state and PL for the A:1s state. The low-energy peak labeled "T" might be related to the trion or phonon replica. (c) Photoluminescence excitation measurements detecting the emission from the A:1s exciton. Peaks related to the resonant excitation of the A:2s and B:1s are marked. (d) Upconversion PL. The laser tuned into resonance with the A:1s state results in emission of about 120 meV higher energy, same as in Fig. 1(d).

energy of 1.96 eV, we also see hot PL emission of this A:2s transition in Fig. 3(b).

To further investigate the nature of these excited exciton states, we carry out PLE experiments. We monitor the PL emission of the A:1s state [as in Fig. 3(b)] as a function of the laser excitation power. PLE probes absorption, which gives information on the higher-lying electronic transitions, and subsequent relaxation to the A:1s state, usually by emitting phonons. In our experiments, we observe clear indications of both processes: absorption by excited exciton states and phonon-assisted energy relaxation. In Fig. 3(c), we see clear resonances in PLE exactly at the same energies as the reflectivity spectrum for the A:2s and B:1s states. The PL emission is enhanced by orders of magnitude where the laser is resonant with these excited exciton states, indicating efficient absorption and energy relaxation. More details on phonon-assisted relaxation and associated Raman scattering on this sample are described in Appendix B.

As discussed in the previous section for $MoSe_2$ MLs, a powerful technique for investigating exciton states is photoluminescence upconversion. Here, a cw laser excites the $MoTe_2$ monolayer at the A:1s resonance, and emission at higher energies is monitored. In Fig. 3(d), we indeed observe emission 120 meV above the A:1s state; this emission is exactly at the same energy as the transition ascribed to the A:2s state with the three other spectroscopy techniques: reflectivity, hot PL, and PLE, which are all compared in Figs. 3(a)–3(d). We note that the upconversion PL of $MoTe_2$ consists of the A:2s emission superimposed on a broad background. The emission of this global upconversion signal increases linearly with laser power and not nearly quadratically as expected. The detection of light emission above the laser excitation energy is clearly a nonlinear process due to the required energy conservation, and we further investigate the reasons for this unexpected power dependence.

IV. ENERGY SEPARATION BETWEEN A:1s AND A:2s STATES

The values of the energy separation between the A:1s and A:2s states,

$$\Delta_{12} \equiv E_{\mathrm{A:2}s} - E_{\mathrm{A:1}s}, \tag{1}$$

obtained by the upconversion spectroscopy and other optical techniques in our experiments are summarized in Table I, together with other excitonic parameters calculated and taken from the literature. As an important result of our measurements, we find that the values of Δ_{12} in hBN-encapsulated $MoSe_2$ and $MoTe_2$ are comparable to the ones in WSe_2 [22,60,61]. The fact that the effective masses of electrons and holes in $MoSe_2$ and $MoTe_2$ are calculated to be about a factor of 2 larger than those in WSe_2 and WS_2 [32] (see also Table I for the summary of values) implies, in principle, values of Δ_{12} in Mo-based monolayers larger than those measured here. However, in two-dimensional semiconductors, the electron-hole interaction law strongly deviates from the $1/r$ dependence due to dielectric screening effects [7,57,58] and can be described by the expression

TABLE I. Exciton parameters obtained in experiments and calculated values. The effective masses of the electron, m_e, and hole, m_h, are taken from Ref. [32] (averaged over different calculation methods and subbands), m_0 is the free electron mass, and $\mu = m_e m_h/(m_e + m_h)$ is the reduced mass of the electron-hole pair; the effective dielectric constant of the surrounding media was chosen as in Ref. [31], $\varkappa = 4.5$; r_0 was chosen to obtain values similar to experimental values of Δ_{12}, Eq. (1). We also present $\rho_0 = \varkappa r_0$, which is used in some references; see Appendix C for details.

	MoS_2	$MoSe_2$	WSe_2	$MoTe_2$
$\Delta_{12}^{\mathrm{exper}}$ (meV)	175	150	130	120
m_e/m_0	0.45	0.53	0.34	0.57
m_h/m_0	0.54	0.6	0.36	0.64
μ/m_0	0.25	0.28	0.17	0.3
r_0 (Å)	6.67	10	8.2	14.4
ρ_0 (Å)	30	45	37	65
E_B^{theor} (meV)	214	186	162	156
$\Delta_{12}^{\mathrm{theor}}$ (meV)	174	148	133	121

$$V(r) = \frac{\pi e^2}{2\varkappa r_0}\left[\mathrm{H}_0\left(\frac{r}{r_0}\right) - \mathrm{N}_0\left(\frac{r}{r_0}\right)\right], \tag{2}$$

where r is the in-plane electron-hole separation, $\varkappa$ is the effective dielectric constants of the surrounding media (taken to be the same for all the structures under study because it is mainly determined by the hBN environment in our encapsulated samples [31]), r_0 is the screening radius, and H_0 and N_0 are the Struve and Neumann functions, respectively. Note that in some references [31,60,62], $\rho_0 = \varkappa r_0$ is used to provide a direct link with the monolayer polarizability. Accounting for this effect by means of a simple variational approach (see Appendix C for details of calculations), we obtain good agreement for the A:1s − A:2s separation; see Table I. Here, the only free parameter is r_0, in reasonable agreement with data in the literature. Note that both measured and calculated separations are in agreement with previous experimental and theoretical results available for WSe_2 and $MoTe_2$; see, e.g., Refs. [31,60,61].

A more detailed understanding of the energy positions of the excited states and more sophisticated modeling may also require going beyond the simple variational scheme, applying various extensions of the screened potential [57,58,60], and accounting for the bands non-parabolicity [63]. The exact values of the effective mass are also discussed in the literature, with interesting new insights from transport measurements in gated samples [64–66], which provide larger values of effective masses.

V. THEORY OF EXCITON UPCONVERSION

To briefly summarize the main experimental results, we have demonstrated that TMD MLs such as $MoTe_2$, $MoSe_2$, MoS_2, and WSe_2 exhibit strong photoluminescence upconversion. At resonant laser excitation of the A:1*s* ground excitonic state, luminescence from *excited* states, such as A:2*s* and B:1*s*, is detected. The effect vanishes for nonresonant excitation or if the oscillator strength of the A:1*s* exciton is reduced by the gate doping in charge tunable samples. Furthermore, the analysis of the upconversion PL intensity as a function of excitation power demonstrates that this effect is nonlinear. In this section, we provide a theoretical model of the upconversion effect observed in TMD MLs. In this process, the emitted photon energy is larger than that of the absorbed photon. That is why, in order to fulfill energy conservation, a third body, an exciton or a phonon, should be involved. However, at a temperature of 4 K, the thermal phonon energies are less than 0.3 meV; thus, lattice vibrations cannot provide effective transfer of excitons up to several 100 meV above the excitation energy. Additionally, the experimental data shown in Fig. 2(c) (see also Ref. [16]) clearly demonstrates the presence of an optical nonlinearity: The upconversion intensity scales quadratically with the number of photoexcited excitons.

A first discussion of possible origins of the upconversion signal can be found in Ref. [16]. The main ingredients are as follows: the absorption of multiple $m \geq 2$ photons and the consequent energy relaxation of photogenerated electron-hole pairs. Further insight into the exact mechanism is provided by the dependence of the upconversion photoluminescence intensity I_{up} on the incident radiation intensity I. The data presented in Fig. 2(c) for the $MoSe_2$ sample [see also published data in Fig. 2(b) of Ref. [16] on WSe_2] show that this dependence is superlinear and roughly scales as $I_{\mathrm{up}} \propto I^{2\alpha}$, where $0.5 < \alpha < 1$. Importantly, the emission from the A:1*s* state under quasiresonant excitation with the same power scales as $I_{\mathrm{A:1}s} \propto I^{\alpha}$, i.e., with a power twice as small. Since the emission intensity is proportional to the occupancy of the corresponding excitonic states, the experimental results demonstrate that the formation of the upconversion signal requires two excitons in the ground state. Hence, the most plausible scenario is related to the exciton-exciton interaction, i.e., the Auger process. This effect is discussed in detail below; we briefly address the other scenarios of upconversion involving direct two-photon absorption and also phonon-assisted processes.

Thus, in order to describe the upconversion theoretically, we need to take into account exciton-exciton interaction processes where one of the excitons is annihilated while the second exciton acquires large extra energy, as depicted in the inset in Fig. 1(b) [67,68]. Subsequently, this exciton relaxes toward the radiative states (particularly, A:2*s* and B:1*s*), and hot luminescence from these states is observed since the radiative recombination time is competitive (i.e., short enough) compared to the energy relaxation time.

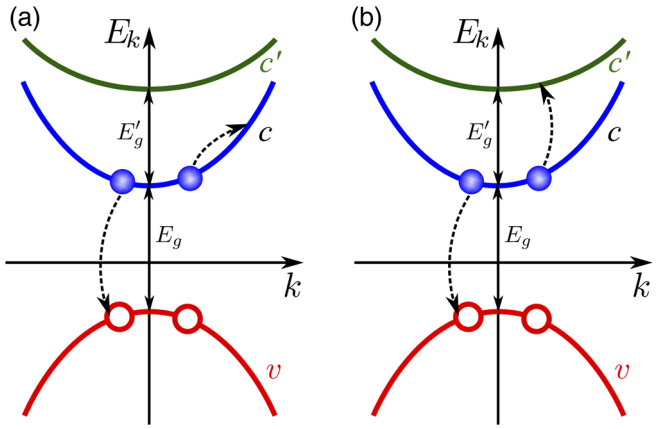

FIG. 4. Model of exciton upconversion—single-particle picture. Filled circles denote electrons; open circles denote unoccupied states in the valence band. Dashed arrows show real electronic transitions. (a) Intraband process enabled by excitonic effects. The resulting high-energy exciton involves carriers in bands c and v; the final momentum $\boldsymbol{K}_f = \boldsymbol{K}_1 + \boldsymbol{K}_2$ is large. (b) Resonant Auger process resulting in high-energy, low-wave-vector $\boldsymbol{K}_f$ excitons involving the excited conduction band c'.

This mechanism of generating highly excited excitons can be viewed as Auger-like exciton-exciton annihilation. At first glance, it seems to be quite weak because, in order to satisfy the energy and momentum conservation laws, the initial kinetic energy of the involved particles should be very large [69,70]. As we show here, this effect is very efficient in TMD MLs due to (i) strong Coulomb interaction, which makes it possible to relax the single-electron momentum conservation [33,34], and (ii) the possibility of resonant processes involving exciton transfer to an excited energy band [16]. In other words, we include the particular energy spacing between different conduction bands in the theory of this four-particle interaction.

The schematics of exciton-exciton Auger processes is presented in Fig. 4. Panel (a) shows an example of a standard Auger process, which is possible in any semiconductor: Because of the Coulomb interaction, one electron recombines with a hole, while another carrier is transferred to a highly excited state. Figure 4(b) illustrates a very different process, which is possible in the studied TMD MLs due to their specific band structure: It turns out that there is an excited conduction band (denoted as c') whose distance to the conduction band, E_g', approximately satisfies the condition

$$E_g' \lesssim E_g - E_B, \tag{3}$$

where $E_B \approx 0.3 \ldots 0.5$ eV [7] is the exciton binding energy for measurements directly on SiO_2 (see Table II), with lower values for E_B of the order of 200 meV in

TABLE II. Band gap energies. Data from DFT calculations summarized in Ref. [71] for S and Se-based MLs and from Ref. [55] for $MoTe_2$ MLs. Here, c' corresponds to the $c+2$ band in the notation of Refs. [32,71]. The direct comparison of the values with experimental data in Fig. 1 is not possible due to the different levels of DFT approximations used.

Energy (eV)	MoS_2	$MoSe_2$	WSe_2	$MoTe_2$
E_g	1.8	1.6	1.7	1.7
E_g'	1.1…1.2	1	1.4	1.3

hBN-encapsulated samples (see Table I and Ref. [61]). Thus, in the course of exciton-exciton annihilation, the electron can be promoted to the c' band with a relatively small wave vector rather than be scattered to a large-wave-vector state within the same band.

The rate of the Auger processes is described by a parameter R_A such that the generation rate of highly energetic excitons is given by

$$\frac{dn_X'}{dt} = R_A n_X^2. \tag{4}$$

Here, n_X' is the density of highly energetic excitons, and n_X is the density of photoexcited excitons in the A:1s state. Recombination and energy relaxation processes are disregarded in Eq. (4). The same rate $R_A n_X^2$ describes the decay rate of A:1s excitons due to the nonradiative exciton-exciton annihilation: $dn_X/dt = -R_A n_X^2$ [33,56,67–69,72–75]. The rate R_A can be expressed by means of the Fermi golden rule in the form

$$R_A = \frac{2\pi}{n_X^2 \hbar} \sum_{\boldsymbol{K}_1,\boldsymbol{K}_2,\nu} |M_{XX}|^2 f(K_1) f(K_2) \times \delta[E_g - 2E_B - E_g' + E(K_1) + E(K_2) - E_\nu(K_f)]. \tag{5}$$

Here, M_{XX} is the matrix element of the exciton-exciton interaction, $\boldsymbol{K}_1$ and $\boldsymbol{K}_2$ are the center-of-mass wave vectors of the two interacting excitons, $f(K)$ is the distribution function of photoexcited A:1s excitons, and $E(K) = \hbar^2 K^2/2M$ is the exciton dispersion, with M being its effective mass. The subscript ν denotes the quantum numbers of the final exciton state, which include the electron band index [c or c' for the processes shown, respectively, in Figs. 4(a) or 4(b)], as well as of the internal motion ($2s, 2p, \ldots$ including the continuum states), and $E_\nu(K)$ is the dispersion of the exciton in the final state, which accounts for its binding energy. The exciton wave vector in the final state, $\boldsymbol{K}_f$, is found from the momentum conservation law: $\boldsymbol{K}_f = \boldsymbol{K}_1 + \boldsymbol{K}_2$. For the derivation of Eq. (5), we assume that the occupation of the final states is negligible and omit the corresponding occupation factor; we also disregard the anisotropy and nonparabolicity of exciton dispersion.

The analytical results are obtained in Appendix D under the model assumptions $E_B \ll E_g, E_g'$, which allow us to make use of $\boldsymbol{k}\cdot\boldsymbol{p}$-perturbation theory for calculating the excitonic states and transition rates [45]. The analysis demonstrates that the dominating contribution to R_A is given by the resonant processes described in Fig. 4(b), where the electron in the exciton is promoted to the excited band c'. The Coulomb interaction between the electrons can result in the process shown in Fig. 4(b), where one pair recombines while the remaining electron occurs in the c' band. So, one $c'v$ pair is present in the end. Since in this process, both electrons change their quantum states, the resonant Auger scattering is due to the electron-electron interaction only, while the electron-hole interaction does not play a role, in contrast to the conventional exciton-exciton scattering where all charge carriers remain in the same bands [76,77]. Moreover, our analysis shows that the exchange contribution to the matrix element dominates; see Appendix D.

Our next goal is to evaluate the scattering rate for excitons under the resonant condition $E_g = E_g' + 2E_B - E_{B,n}$, where the energy released at the nonradiative recombination of the A:1s exciton with $\boldsymbol{K} = 0$ is equal to the energy of the excited c'-band exciton in the ns state. To that end, the distribution function $f(K)$ of excitons should be determined. It is controlled by the interplay of the generation process and all types of relaxation processes, including exciton-exciton and exciton-phonon scattering as well as the radiative decay for the excitons with small wave vector K within the radiative cone and the redistribution of excitons between the bright and dark (spin-forbidden) states. The generation rate of the excitons under the resonant excitation used in our experiments can be recast in the resonant form as [cf. Eq. (E2) and Refs. [16,44]]

$$\left.\frac{dn_X}{dt}\right|_{\text{gen}} \propto \frac{1}{(\hbar\omega - E_{\text{A:1}s})^2 + \hbar^2\Gamma_A^2} \frac{I}{\hbar\omega}, \tag{6}$$

where $E_{\text{A:1}s} = E_g - E_B$ is the resonant energy of the A:1s exciton, and Γ_A is the damping rate of this exciton. Here, we abstain from presenting and solving the full kinetic equation model for exciton distribution and analyze the timescales of the most important processes. The calculations [44,78–80] show that, at cryogenic temperatures of $2, \ldots, 4$ K, the exciton-acoustic phonon scattering time is in the picosecond timescale, i.e., on the same order of magnitude as the radiative decay rate. Thus, even at low temperatures, photocreated excitons can efficiently leave the light cone to the nonradiative states. Additionally, as recently shown [44,80], the pronounced high-energy tails in the exciton absorption are caused by the exciton-phonon interaction, which can be accounted for by the ω-dependent Γ_A in Eq. (6). These tails are also quite visible in the upconversion excitation spectra,

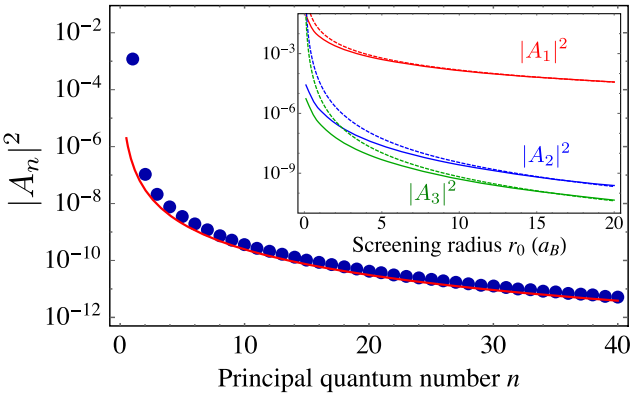

FIG. 5. Dependence of the coefficient $|A_n|^2$ on n for $r_0 = 3a_B$. The red line shows the approximation $|A_n|^2 = 2.47 \times 10^{-7}/n^3$. The inset shows dependences $|A_1|^2$ (red), $|A_2|^2$ (blue), and $|A_3|^2$ (green) on the screening radius r_0. Dashed lines are fits $|A_1|^2 = 0.015(a_B/r_0)^2$, $|A_2|^2 = 3.46 \times 10^{-5}(a_B/r_0)^4$, and $|A_3|^2 = 6.63 \times 10^{-6}(a_B/r_0)^4$.

Fig. 2(d); such processes can efficiently generate the excitons with large wave vectors and kinetic energies [44]. In contrast, the rate of exciton-exciton Auger annihilation is about an order of magnitude smaller; see Appendix D and below. Thus, excitons are likely to thermalize [81].

Finally, neglecting the difference of exciton masses in the initial and final states and assuming, on the basis of the arguments above, that excitons are thermalized with the temperature T, we have

$$R_A = \frac{\pi}{\hbar k_B T}\left|\frac{2\pi e^2 \gamma_3 \gamma_6}{\varkappa a_B^2 E_g E_g'}\right|^2 |A_n|^2. \tag{7}$$

Here, k_B is the Boltzmann constant, a_B is the exciton Bohr radius, γ_3 and γ_6 are the interband momentum matrix elements (in units of $m_0/\hbar$, m_0 being the free electron mass) for electron transition from c to, respectively, v and c' bands, and $\varkappa$ is the effective high-frequency dielectric constant. In Eq. (7), A_n is the dimensionless overlap integral, which depends on the screening parameter r_0 in the interaction potential (2); see Appendix D for details. The values of $|A_n|^2$ for several excitonic states are shown in Fig. 5. For $n = 1$ and reasonable material parameters [71], the quantity R_A at $T = 4$ K in Eq. (7) can be estimated to be $1, \ldots, 10$ cm^2/s. This quantity can be reduced by a factor $10, \ldots, 100$ if the resonant condition is not fulfilled. The rate of intraband transitions, where the electron remains in the same band, Fig. 4(a), can be estimated by replacing the factor $\gamma_6/(a_B E_g')$ by $(E_B/E_g)^{3/2}$, which produces a parametrically smaller, $\sim E_B/E_g$ contribution; see Appendix D. In the nonresonant case the transition at $K_1 = K_2 = 0$ is not possible, and the detuning $\Delta = E_g' - E_g + 2E_B - E_{B,n}$ is present for the intraband process. This intraband process is only possible when excitons with the kinetic energy on the order of Δ are present. The rate equation (7) therefore acquires an exponential factor $\exp(-|\Delta|/k_B T) < 1$.

The experimentally observed Auger rates in the literature are 1–2 orders of magnitude smaller than the resonant contribution to R_A investigated here [67,68,72–75,82]. The exact values of R_A will also vary with sample temperature and environment, demonstrating that the exact resonance conditions are not fulfilled in the studied structures. Furthermore, depending on the material, e.g., for W-based monolayers, a considerable part of the excitonic population can be in the spin-dark states, which also affects the Auger rates because, for the Auger process, at least one exciton should be spin allowed. Our experiments are carried out at 4 K, whereas many exciton-exciton scattering studies are carried out at elevated temperatures. The presence of disorder in the sample, especially without hBN encapsulation, may enable us to simultaneously fulfill the energy and momentum conservation in TMD MLs, making additional scenarios possible.

Let us briefly address other possible origins of the upconversion effect. The straightforward one is due to the hot photoluminescence excited by two-photon absorption. The details of the process are given in Appendix E. The estimates show that this process is about 3 orders of magnitude weaker than the resonant Auger process described above. Moreover, strictly speaking, it is characterized by the $I_{\mathrm{up}} \propto I^2$ dependence, in contrast to the experimental data. However, the present analysis cannot fully rule out such a process or more sophisticated processes, where the exciton-phonon interaction is involved at one of the steps of the two-photon absorption. The detailed calculation of the rates of these processes can be superficial because of the imprecise knowledge of the band-structure parameters and, therefore, the impossibility to check to which extent all needed resonance conditions are fulfilled. We believe that this analysis will stimulate further experimental and theoretical studies aimed, in particular, at specifying band parameters of two-dimensional materials.

To summarize, our analysis suggests that exciton upconversion photoluminescence in TMD MLs is possibly due to a specific nonlinear process: Two excitons generated by the resonant laser collide; as a result, one of those excitons recombines nonradiatively, while the other is promoted to a highly excited state (most likely related to an excited conduction subband according to the band-structure calculation). Subsequently, the excited exciton loses its energy, and a hot PL from the radiative A:2s and B:1s states is observed. This scenario describes the main experimental findings: (i) upconversion PL from the states A:2s and B:1s, which are visible in the hot PL [Figs. 1, 2(a), 2(b), 2(d), and 3], (ii) quadratic dependence of the upconversion intensity on the number of excitons in the ground state, Fig. 2(c), (iii) resonant character of the process as a function of excitation laser energy, Fig. 2(d), and (iv) absence of the upconversion in the presence of doping, where the exciton resonance vanishes, Fig. 2(f).

VI. CONCLUSION

We identify excited exciton states in high-quality $MoSe_2$ and $MoTe_2$ monolayer samples, which govern absorption and emission above the A:1s exciton resonance. We also identify the A:2s state 150 meV (120 meV) above the A:1s state in ML $MoSe_2$ ($MoTe_2$). We show that excited exciton states can be studied in photoluminescence upconversion experiments. In addition to being a highly selective spectroscopic tool applicable to several TMD materials [16,31], this nonlinear optical effect also gives insights into exciton-exciton interactions—relevant physical processes that are also used for studying population inversion and other density-dependent phenomena [75,83–85]. We discuss the possibility that, in TMD monolayers, the generation of high-energy excitons with Auger-like scattering processes is efficient due to the strong Coulomb interaction and resonant excitation of higher-lying conduction bands.

ACKNOWLEDGMENTS

We acknowledge funding from ANR 2D-vdW-Spin, ANR VallEx, Labex NEXT projects VWspin and MILO, ITN Spin-NANO Marie Sklodowska-Curie Grant Agreement No. 676108, and ITN 4PHOTON No. 721394. X. M. also acknowledges the Institut Universitaire de France. Growth of hexagonal boron nitride crystals was supported by the Elemental Strategy Initiative conducted by the MEXT, Japan and the CREST (JPMJCR15F3), JST. L. E. G. and M. M. G. acknowledge partial support from LIA ILNACS, RFBR Projects No. 17-02-00383 and No. 17-52-16020, Russian Federation President Grant No. MD-1555.2017.2, and the BASIS Foundation.

APPENDIX A: EXPERIMENTAL METHODS

The samples are fabricated by mechanical exfoliation of bulk $MoSe_2$ and $MoTe_2$ (commercially available from 2D semiconductors) and very-high-quality hexagonal boron nitride (hBN) crystals [40] on 83-nm SiO_2 on a Si substrate. The experiments are carried out at $T = 4$ K in a confocal microscope built in a vibration-free, closed-cycle cryostat. The excitation/detection spot diameter is $\sim 1\ \mu$m. The monolayer (ML) is excited by a continuous-wave Ti-Sa laser (700–1020 nm) or a HeNe laser (633 nm). The PL signal is dispersed in a spectrometer and detected with a Si-CCD camera ($\lambda < 1\ \mu$m) or InGaAs detector ($\lambda > 1\ \mu$m). The typical excitation power is 3 μW.

APPENDIX B: ADDITIONAL DATA

Charge tuning in ML $MoSe_2$.—Figure 6 demonstrates the reflectivity spectrum of the charge tunable $MoSe_2$ device clearly showing the redistribution of the oscillator strength between the neutral and charged excitons, which is studied in the context of upconversion in Figs. 2(e) and 2(f).

Resonant and nonresonant Raman scattering in ML $MoTe_2$.—Scattering with phonons in Raman processes

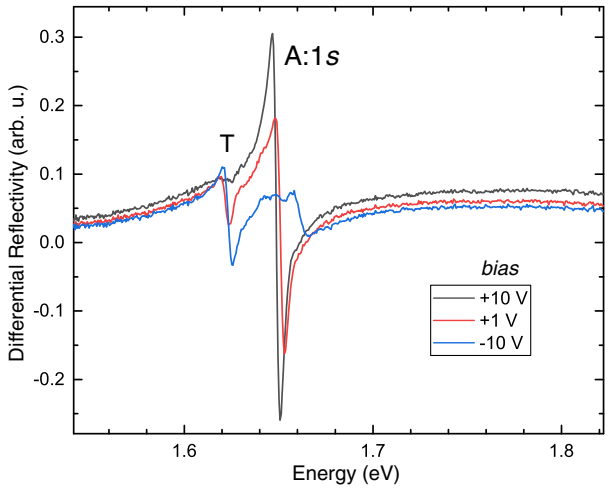

FIG. 6. Charge tunable device. In differential reflectivity on the charge tunable device of Figs. 2(e) and 2(f), we identify the A:1s state and, at more negative bias, the charged exciton state (marked T for trion).

allows us to distinguish monolayers from multilayers. This is especially useful for $MoTe_2$, where the bilayer also shows clear and narrow PL emission. In Fig. 7a, we compare results for a monolayer and a bilayer, the absence of the low-energy A_{1g} peak allows us to identify monolayer samples [86,87]. The experiments in Fig. 7a are essentially based on nonresonant Raman scattering; i.e., neither the laser energy nor the emitted light after phonon scattering is resonant with a particular electronic state. This is different in Fig. 7b: Here, we tune the laser to an excess energy of about 20 meV above the A:1s resonance. In addition to PL emission (orange peak), we see a spectrally sharper feature (shaded blue) superimposed on the PL, which shifts with excitation laser energy. This peak corresponds to Raman scattering with the A_1' phonon, which is particularly efficient as the final state after scattering corresponds to a real electronic state [17,86,88–91] in these single-resonant Raman scattering experiments.

In Fig. 7c, we report double-resonant Raman experiments [22,89]. As the laser energy is scanned across the A:2s state, we see that the PL of the A:1s exciton is enhanced; see intensity plotted in Fig. 3(c) as a function of laser energy. In addition, we observe in Fig. 7c that a Raman feature is crossing the PL line, exactly 120 meV below the respective laser energy. When the laser is at the A:2s energy, the Raman process is double resonant [86,89] as the initial state (A:2s) and the final state (A:1s) are real electronic states. This case has already been observed between exciton states in ML WSe_2 on SiO_2 [89]. Please note that very different electronic states and phonons are discussed in the double-resonant Raman experiments in Ref. [86]. Detailed $MoTe_2$ Raman studies are also reported for monolayers and multilayers in Ref. [48]. In experiments in hBN-encapsulated ML WSe_2 samples, similar experiments

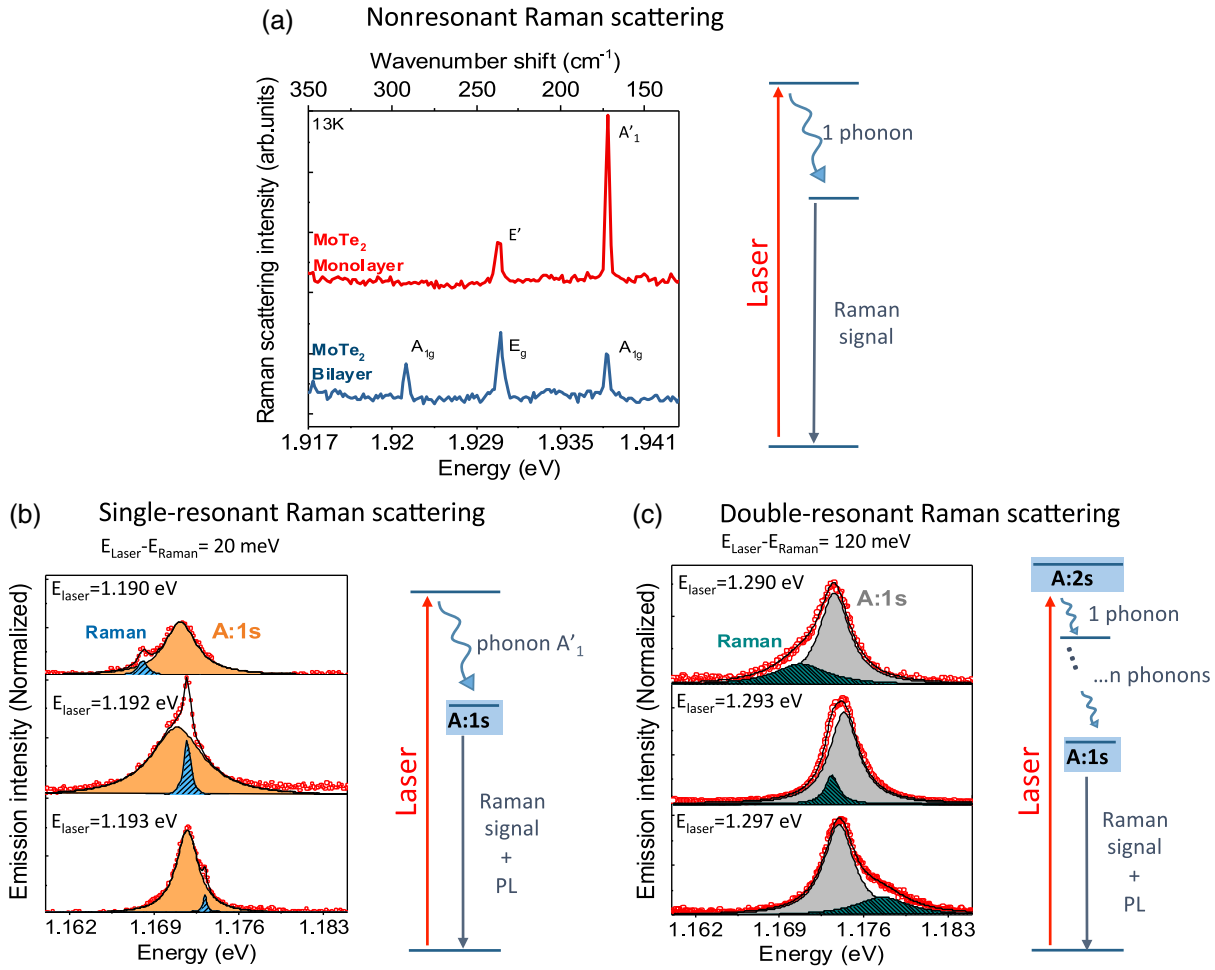

FIG. 7. Raman spectroscopy in ML $MoTe_2$, $T = 4$ K. (a) Nonresonant Raman scattering using a HeNe laser. (b) Single-resonant Raman scattering as the excitation laser energy is one phonon energy A_1' above the A:1s state. (c) Double-resonant Raman experiments, as a phonon multiple ensures efficient relaxation from the optically excited A:2s state to the emitting A:1s state.

have been interpreted as being due to phonon-related processes only [15]. This interpretation seems unlikely in view of follow-up studies of ML WSe_2 in magnetic fields, which clearly showed that the excited state is an excitonic transition and not just a phonon replica [61]. For the case of $MoTe_2$, we have a strong case for the transition at 120 meV above the A:1s to be attributed to a real electronic transition, as this transition is confirmed in Figs. 3(a)–3(d) by four complementary spectroscopy techniques and in Fig. 7c by double-resonant Raman scattering.

APPENDIX C: BINDING ENERGIES OF EXCITONIC STATES IN VARIATIONAL APPROACH

In order to calculate the energy separation between the ground and excited excitonic states, we apply a simple variational approach. The wave functions of the ground and first excited states are sought in the two-dimensional hydrogenic form

$$\Phi_{1s}(r) = \sqrt{\frac{2}{\pi a^2}} e^{-r/a}, \tag{C1a}$$

$$\Phi_{2s}(r) = \sqrt{\frac{2}{27\pi a^2}} \left(1 - \frac{2r}{3a}\right) e^{-r/3a}, \tag{C1b}$$

with the only trial parameter a, which is the same for both functions. Such an approach has the advantage of automatically providing orthogonal ground and excited states at the cost of simplicity. To test the calculation, we reproduce, within an error of $\leq 2\%$, the results of Ref. [31], where more sophisticated numerical approaches were used, for A:1s and A:2s excitons in the monolayer of MoS_2 with the same set of band structure and screening parameters.

APPENDIX D: CALCULATION OF AUGER RATES

1. Resonant interband process

We consider three bands, c, v, c', schematically illustrated in Fig. 4 with two excited electron-hole pairs (excitons) with

an electron occupying the lowest conduction band c and with an empty state in the valence band v. Here, for simplicity, we disregard the spin degree of freedom of change carriers, assuming that the spin is conserved in the course of exciton-exciton interaction. Furthermore, we focus on the states in the vicinity of one of the band extrema ($\boldsymbol{K}_+$ or $\boldsymbol{K}_-$ valley) and disregard the processes involving intervalley transfer of electron-hole pairs studied in Refs. [92]. The Coulomb interaction between the electrons can result in the process shown in Fig. 4(b), where one pair recombines while the remaining electron occurs in the c' band. So, one $c'v$ pair is present in the end. Since in this process both electrons change their quantum states, the resonant Auger scattering is due to the electron-electron interaction only, while, e.g., electron-hole interaction does not play a role.

In the free-particle picture, we have two electrons in the c band, which occur in the c' and v bands after Coulomb scattering. The two-electron wave functions of the considered system in the initial and final states can be presented as

$$|i\rangle = \frac{1}{\sqrt{2}}[\Psi_{c\boldsymbol{k}_c}(\boldsymbol{r}_1)\Psi_{c\tilde{\boldsymbol{k}}_c}(\boldsymbol{r}_2) - \Psi_{c\boldsymbol{k}_c}(\boldsymbol{r}_2)\Psi_{c\tilde{\boldsymbol{k}}_c}(\boldsymbol{r}_1)],$$
$$|f\rangle = \frac{1}{\sqrt{2}}[\Psi_{v\boldsymbol{k}_v}(\boldsymbol{r}_1)\Psi_{c'\boldsymbol{k}_{c'}}(\boldsymbol{r}_2) - \Psi_{v\boldsymbol{k}_v}(\boldsymbol{r}_2)\Psi_{c'\boldsymbol{k}_{c'}}(\boldsymbol{r}_1)]. \quad \text{(D1)}$$

Here, $\boldsymbol{k}_c$, $\boldsymbol{k}_v$ are the electron and unoccupied-state wave vectors in one of the excitons, and $\tilde{\boldsymbol{k}}_c$, $\tilde{\boldsymbol{k}}_v$ are the electron and unoccupied-state wave vectors in another exciton. The wave function in each band $n = c$, c', v is a product of the Bloch amplitude and the plane wave:

$$\Psi_{n\boldsymbol{k}}(\boldsymbol{r}) = e^{i\boldsymbol{k}\cdot\boldsymbol{r}}u_{n\boldsymbol{k}}(\boldsymbol{r}), \quad \text{(D2)}$$

and the normalization area is set to unity. In the $\boldsymbol{k}\cdot\boldsymbol{p}$ model, the Bloch amplitudes have the form

$$u_{c\boldsymbol{k}_c} = u_c + \frac{\hbar}{m_0}\frac{\boldsymbol{k}_c\cdot\boldsymbol{p}_{vc}}{E_c - E_v}u_v + \frac{\hbar}{m_0}\frac{\boldsymbol{k}_c\cdot\boldsymbol{p}_{c'c}}{E_c - E_{c'}}u_{c'}, \quad \text{(D3)}$$

$$u_{c'\boldsymbol{k}_{c'}} = u_{c'} + \frac{\hbar}{m_0}\frac{\boldsymbol{k}_{c'}\cdot\boldsymbol{p}_{vc'}}{E_{c'} - E_v}u_v + \frac{\hbar}{m_0}\frac{\boldsymbol{k}_{c'}\cdot\boldsymbol{p}_{cc'}}{E_{c'} - E_c}u_c, \quad \text{(D4)}$$

$$u_{v\boldsymbol{k}_v} = u_v + \frac{\hbar}{m_0}\frac{\boldsymbol{k}_v\cdot\boldsymbol{p}_{cv}}{E_v - E_c}u_c + \frac{\hbar}{m_0}\frac{\boldsymbol{k}_v\cdot\boldsymbol{p}_{c'v}}{E_v - E_{c'}}u_{c'}, \quad \text{(D5)}$$

where u_n denotes the Bloch amplitude at the extremum point, m_0 is the free electron mass, and $\boldsymbol{p}_{nn'}$ are the momentum matrix elements between the states in the bands n and n' (n, $n' = c$, c', v).

The wave functions $|i\rangle$, $|f\rangle$ in Eq. (D1) are antisymmetrized with respect to the permutations of electrons, giving rise to the *direct* and *exchange* contributions. The matrix element of the direct interaction, where the electron from the state with the wave vector $\boldsymbol{k}_c$ recombines with the hole from the same exciton and transfers to the state $\boldsymbol{k}_v$, can be conveniently presented in the form

$$M_{\mathrm{dir}} = \langle u_{v\boldsymbol{k}_v}|u_{c\boldsymbol{k}_c}\rangle\langle u_{c'\boldsymbol{k}_{c'}}|u_{c\tilde{\boldsymbol{k}}_c}\rangle \times V_C(K_1)\delta_{\boldsymbol{K}_1,\boldsymbol{k}_c-\boldsymbol{k}_v}\delta_{\boldsymbol{K}_1,\boldsymbol{k}_{c'}-\tilde{\boldsymbol{k}}_c}, \quad \text{(D6)}$$

where $\boldsymbol{K}_1 = \boldsymbol{k}_c - \boldsymbol{k}_v$ is the exciton center-of-mass momentum (note that the hole state corresponds to the time-reversed counterpart of the unoccupied state) and

$$V_C(q) = \frac{2\pi e^2}{\varkappa q(1 + qr_0)} \quad \text{(D7)}$$

is the 2D Fourier image of the Coulomb potential, with $\varkappa$ being the background average constant of the surrounding structure and r_0 being the dielectric screening parameter [57,58,93]. Note that this parameter should be taken in the high-frequency limit because the energy transferred in the course of the exciton-exciton interaction is on the order of the band gap E_g.

Taking into account that

$$\frac{\hbar}{m_0}\boldsymbol{k}\cdot\boldsymbol{p}_{vc} = \gamma_3^* k_+, \qquad \frac{\hbar}{m_0}\boldsymbol{k}\cdot\boldsymbol{p}_{c'c} = \gamma_6 k_-, \quad \text{(D8)}$$

where γ_3 and γ_6 are the band-structure parameters introduced in Refs. [32,71] and $k_\pm = k_x \pm ik_y$, we obtain

$$\langle u_{v\boldsymbol{k}_v}|u_{c\boldsymbol{k}_c}\rangle = \frac{\gamma_3^* K_+}{E_c - E_v}, \qquad \langle u_{c'\boldsymbol{k}_{c'}}|u_{c\tilde{\boldsymbol{k}}_c}\rangle = \frac{\gamma_6 K_-}{E_{c'} - E_c}. \quad \text{(D9)}$$

Finally, the direct interaction matrix element takes a simple form

$$M_1(K_1) \equiv V_C(K_1)\frac{\gamma_3^*\gamma_6 K_1^2}{E_g E_g'}\delta_{\boldsymbol{K}_1,\boldsymbol{k}_c-\boldsymbol{k}_v}\delta_{\boldsymbol{K}_1,\boldsymbol{k}_{c'}-\tilde{\boldsymbol{k}}_c}. \quad \text{(D10)}$$

Taking into account the excitonic effect, Eq. (D10) should be averaged over the exciton wave function [45,92,94]. Furthermore, we need to note that, in the initial state, there are two unoccupied states in the valence band. As a result, we have (K_1, $K_2 \ll a_B^{-1}$)

$$M_{\mathrm{dir}}(\boldsymbol{K}_1, \boldsymbol{K}_2, \boldsymbol{K}_f, n) = \delta_{\nu,1s}\delta_{\boldsymbol{K}_f,\boldsymbol{K}_1+\boldsymbol{K}_2}\Phi_{1s}(0) \times \frac{1}{2}[V_C(K_1)K_1^2 + V_C(K_2)K_2^2]\frac{\gamma_3^*\gamma_6}{E_g E_g'}. \quad \text{(D11)}$$

We recall that $\boldsymbol{K}_1, \boldsymbol{K}_2$ are the wave vectors of excitons in the initial state, $\boldsymbol{K}_f = \boldsymbol{K}_1 + \boldsymbol{K}_2$ is the wave vector of the exciton in the final state, and the subscript ν enumerates the relative motion states of the remaining electron-hole pair. In the derivation of Eq. (D11), we neglected the difference of the electron effective masses in c and c' bands and assumed that, initially, both excitons occupy $1s$ state; $\Phi_{1s}(\rho)$ is the

envelope function of the relative motion. Correspondingly, the final-state relative motion envelope function remains the same.

The typical center of mass wave vectors involved in exciton-exciton scattering are on the order of the thermal wave vector $K_T = \sqrt{2Mk_BT/\hbar^2}$ and are much smaller than the screening wave vector r_0^{-1}; therefore, the direct exciton-exciton scattering matrix element $M_{\rm dir}$ is proportional to the first powers of the exciton wave vectors: $M_{\rm dir} \propto K_T$.

Next, we consider an exchange process, where the electron occupies the empty state in the valence band related to the hole in the other exciton; i.e., the electron with the wave vector $\boldsymbol{k}_c$ transfers to the valence band state with the wave vector $\tilde{\boldsymbol{k}}_v$. As a result, for uncorrelated electron-hole pairs, we have

$$-M_1(|\boldsymbol{k}_c - \tilde{\boldsymbol{k}}_v|), \tag{D12}$$

for the exchange contribution, where M_1 is defined in Eq. (D10). In order to transform Eq. (D12) to the form convenient for averaging over the exciton wave functions, we introduce the relative motion wave vectors for two initial and final exciton states in accordance with

$$\boldsymbol{k}_1 = \frac{\boldsymbol{k}_c + \boldsymbol{k}_v}{2}, \qquad \boldsymbol{k}_2 = \frac{\tilde{\boldsymbol{k}}_c + \tilde{\boldsymbol{k}}_v}{2},$$
$$\boldsymbol{k}_f = \frac{\boldsymbol{k}_{c'} + \boldsymbol{k}_v}{2} = \boldsymbol{k}_1 + \frac{\boldsymbol{K}_2}{2}. \tag{D13}$$

Here, we assumed that the effective masses of the electron and hole are the same, in agreement with microscopic calculations [32,71], see also Table II. Taking into account that, as before, the center-of-mass wave vectors K_1, $K_2 \sim K_T$ are small compared with the inverse Bohr radius a_B^{-1} of the exciton, we omit $\boldsymbol{K}_f$ in $\boldsymbol{k}_c - \tilde{\boldsymbol{k}}_v = \boldsymbol{k}_1 - \boldsymbol{k}_2 + \boldsymbol{K}_f/2$ and in $\boldsymbol{k}_1 + \boldsymbol{K}_f/2$ and arrive at

$$M_{\rm exch}(\boldsymbol{K}_1, \boldsymbol{K}_2, \boldsymbol{K}_f, \nu) \approx -\delta_{\boldsymbol{K}_f, \boldsymbol{K}_1+\boldsymbol{K}_2} \times \sum_{\boldsymbol{k}_1, \boldsymbol{k}_2} M_1(|\boldsymbol{k}_1 - \boldsymbol{k}_2|) C_\nu^*(\boldsymbol{k}_1) C_{1s}(k_2) C_{1s}(k_1). \tag{D14}$$

Here, $C_\nu(\boldsymbol{k})$ are the Fourier transforms of the relative motion exciton functions $\Phi_\nu(\boldsymbol{\rho})$:

$$C_\nu(\boldsymbol{k}) = \int d\boldsymbol{\rho} e^{i\boldsymbol{k}\cdot\boldsymbol{\rho}} \Phi_\nu(\boldsymbol{\rho}).$$

It follows from Eq. (D14) that only s-shell states contribute to the matrix element. As compared with its direct counterpart, the transferred momentum here is $|\boldsymbol{k}_1 - \boldsymbol{k}_2| \sim a_B^{-1}$. Since $M_1(q) \propto q$ for $qr_0 \ll 0$, the direct contribution is by a factor $K_T a_B$ smaller than the exchange one. Thus, in what follows, we consider the exchange contribution only.

In order to analyze the exchange process in more detail, we first consider a limit where the screening is very strong, i.e., where $|\boldsymbol{k}_1 - \boldsymbol{k}_2| r_0 \gg 1$. In this case, we can approximate $M_1(q)$ by a constant and arrive at

$$M_{\rm exch}(\boldsymbol{K}_1, \boldsymbol{K}_2, \boldsymbol{K}_f, \nu) \approx -\delta_{\nu,1s}\delta_{\boldsymbol{K}_f, \boldsymbol{K}_1+\boldsymbol{K}_2} \frac{2\pi e^2}{\varkappa r_0} \frac{\gamma_3^*\gamma_6}{E_g E_g'} \Phi_{1s}(0). \tag{D15}$$

For arbitrary screening, we evaluate the sum in Eq. (D14), making use of the two-dimensional hydrogenic functions. For the bound states $\nu = ns$, we have [95]

$$C_{ns}(k) = 2\sqrt{2\pi} a_B \left(\frac{2n-1}{1+\kappa_n^2}\right)^{3/2} P_{n-1}\left(\frac{\kappa_n^2 - 1}{\kappa_n^2 + 1}\right), \tag{D16}$$

with $\kappa_n = (2n-1)ka_B$ and $P_n(x)$ being the Legendre polynomial. As a result,

$$M_{\rm exch}(\boldsymbol{K}_1, \boldsymbol{K}_2, \boldsymbol{K}_f, ns) = \frac{A_n(r_0)}{a_B^2} \frac{2\pi e^2 \gamma_3^* \gamma_6}{\varkappa E_g E_g'} \delta_{\boldsymbol{K}_f, \boldsymbol{K}_1+\boldsymbol{K}_2}. \tag{D17}$$

Dependence of $|A_n|^2$ on n for $r_0 = 3a_B$ is shown in Fig. 5. We see that the squared matrix element decreases rapidly with n. It follows from Eq. (D16) that $C_{n0} \propto n^{-3/2}$ at $n \to \infty$; therefore, $|M_b|^2 \sim n^{-3}$. Figure 5 shows that this asymptotic is valid already at $n \geq 3$.

The inset to Fig. 5 shows the dependences of the scattering probability on the screening radius r_0. Final states with $n = 1, 2, 3$ are considered. As mentioned above, scattering into the ns state for the short-range interaction is possible at $n = 1$ only. The probability of this process decreases as $1/r_0^2$, while for $n \geq 2$, it drops as $1/r_0^4$. The corresponding asymptotes are shown by dashed lines in Fig. 5.

2. Intraband Auger process

Let us now briefly address the intraband process depicted in Fig. 4(a), where the charge carriers remain in the same bands after the scattering. For free carriers, the process has a high threshold, requiring the initial and final wave vectors to be on the order of $\sqrt{ME_g/\hbar^2}$; otherwise, the energy and momentum conservation laws cannot be satisfied simultaneously. Taking into account the excitonic effect, the process becomes allowed because one can find, in the relative motion wavefunction Fourier image [Eq. (D16)], sufficiently large wave vectors due to the Coulomb interaction. In other words, the electron-hole Coulomb interaction either in the initial or in the final state may relax the momentum conservation in the course of the Auger scattering. However, the two-band

approximation is insufficient to give a correct result since (i) the model approximations for the band dispersions are, as a rule, invalid at the kinetic energies $\sim E_g$ due to the $\boldsymbol{k}\cdot\boldsymbol{p}$ interaction with remote bands [32,69] and (ii) the asymptotic form of $C_v(k)$ at large wave vectors can strongly differ from a simplified hydrogenic model (D16) [7,12,94]. Thus, we present only analytical estimations based on the parabolic approximations for the band dispersions, assuming that the ratio E_g/E_B is very large, which allows us to take into account the Coulomb effects perturbatively.

We start from the direct process. Instead of Eq. (D10), we have, for the free carrier scattering,

$$V_C(K_1)\frac{\gamma_3^* K_{1,+}}{E_g}\delta_{\boldsymbol{K}_1,\boldsymbol{k}_c-\boldsymbol{k}_v}\delta_{\boldsymbol{K}_1,\boldsymbol{k}_{c'}-\tilde{\boldsymbol{k}}_c}. \tag{D18}$$

As compared with Eq. (D10), the factor $\propto \gamma_6/E_g'$ is absent due to the fact that only one charge carrier changes the band. Making use of the following notations,

$$\begin{aligned}\boldsymbol{k}_{c'} &= \boldsymbol{k}_f + \frac{\boldsymbol{K}_1+\boldsymbol{K}_2}{2} = \boldsymbol{k}_f + \frac{\boldsymbol{K}_f}{2},\\ \tilde{\boldsymbol{k}}_c &= \boldsymbol{k}_f + \frac{\boldsymbol{K}_2-\boldsymbol{K}_1}{2},\end{aligned} \tag{D19}$$

we obtain, for the exciton Auger scattering matrix element, the following expression:

$$\begin{aligned}M'_{\rm dir}(\boldsymbol{K}_1,\boldsymbol{K}_2,\boldsymbol{K}_f,\boldsymbol{k}_f) &= \delta_{\boldsymbol{K}_f,\boldsymbol{K}_1+\boldsymbol{K}_2}\Phi_{1s}(0)\frac{V_C(K_1)\gamma_3^* K_{1,+}}{E_g}\\ &\times\int d\boldsymbol{r}\,e^{i\boldsymbol{K}_1\cdot\boldsymbol{r}/2}\Phi^*_{k_f,l}(\boldsymbol{r})\Phi_{1s}(\boldsymbol{r})\\ &+\boldsymbol{K}_1\leftrightarrow\boldsymbol{K}_2.\end{aligned} \tag{D20}$$

Here, we take into account that only excitons with positive energies of relative motion can be in the final state; i.e., $\boldsymbol{k}_f$ corresponds to the continuum electron-hole pair state modified by the Coulomb interaction. The final-state wave vector can be estimated from the energy conservation condition with the result $k_f=\sqrt{(E_g-2E_B)M/(2\hbar^2)}$. In this estimate, we neglect thermal energy of excitons as compared with E_g-2E_B and, as before, take the same effective masses for an electron and a hole.

Since $K_1 \ll a_B^{-1}$, k_f, the integral in Eq. (D20) can be evaluated by decomposing the exponent in the series. At $K_1=0$, the integral in Eq. (D20) equals zero due to orthogonality of the functions of discrete and continuous spectra. Therefore, we take into account the K_1-linear term:

$$\int d\boldsymbol{r}\,e^{i\boldsymbol{K}_1\cdot\boldsymbol{r}/2}\Phi^*_{k_f,l}(\boldsymbol{r})\Phi_{1s}(\boldsymbol{r}) \approx a_B K_1 D(k_f), \tag{D21}$$

where

$$D(k_f)=\frac{ia_B}{2}\int d\boldsymbol{r}\,r\cos\varphi\Phi^*_{k_f,1}(\boldsymbol{r})\Phi_{1s}(r)\ll 1. \tag{D22}$$

Within the hydrogenic model, which is used hereafter for crude estimations, $D(k_f)\propto(k_f a_B)^{-3}$ and the ratio of the interband contribution (D11) and the intraband contribution (D20) can be estimated as

$$\left|\frac{M_{\rm dir}}{M'_{\rm dir}}\right| \sim \frac{\gamma_6}{a_B E_g'}\left(\frac{E_g}{E_B}\right)^{3/2} \sim \frac{E_g}{E_B}\gg 1. \tag{D23}$$

Thus, the resonant interband process is dominant. A similar estimate holds for the exchange contributions.

3. Auger recombination rate

The exciton Auger recombination rate at resonant interband scattering of two $1s$ excitons into the ns exciton state is given by [cf. Eq. (5) of the main text]

$$\begin{aligned}R_A n_X^2 = \frac{2\pi}{\hbar}\sum_{\boldsymbol{K}_1,\boldsymbol{K}_2}&|M_{\rm exch}(\boldsymbol{K}_1,\boldsymbol{K}_2,\boldsymbol{K}_f,ns)|^2 f(K_1)f(K_2)\\ &\times\delta[E_g-2E_B-E_g'+E(K_1)+E(K_2)-E_{ns}(K_f)].\end{aligned} \tag{D24}$$

In order to calculate the rate of transitions, we take into account that the matrix element $M_{\rm exch}(\boldsymbol{K}_1,\boldsymbol{K}_2,\boldsymbol{K}_f,ns)$ depends on the principal quantum number n of the final state and is independent of the initial wave vectors of excitons.

Let us first assume that there is exact resonance; i.e., for a certain value of n at $\boldsymbol{K}_1=\boldsymbol{K}_2=\boldsymbol{K}_f$, we have

$$E_g = E_g' + 2E_B - E_{B,n}, \tag{D25}$$

where $E_{B,n}$ is the binding energy of the ns state. Removing the energy conservation δ function and assuming that

$$f(K)=\mathcal{N}\exp\left(-\frac{\hbar^2K^2}{2Mk_BT}\right), \tag{D26}$$

i.e., that the excitons are distributed according to the Boltzmann law at the temperature T, and $\mathcal{N}$ is the normalization constant determined by the condition

$$n_X = g\sum_{\boldsymbol{K}} f(K),$$

where the factor g accounts for the spin and valley degeneracy, we have

$$R_A = R_n, R_n = \frac{\pi}{\hbar k_B T}\left|\frac{2\pi e^2 A_n \gamma_3^*\gamma_6}{\varkappa a_B^2 E_g E_g'}\right|^2. \tag{D27}$$

Note that the Auger process is active for collisions of bright (spin-allowed) excitons with bright or dark ones, while for

the dark-dark scattering, the process is strongly suppressed. In the latter case, the $\boldsymbol{k}\cdot\boldsymbol{p}$ admixture with the valence band is minor, and the recombination via the discussed channel is not effective. The Auger decay rate can be recast in the alternative form

$$R_A n_X^2 \equiv \frac{n_X}{\tau_A}, \tag{D28}$$

where we introduced the Auger recombination time $\tau_A(n_X)$. Since $e^2/a_B \sim E_B$, we have an estimate in the case of the resonance with the $1s$ state

$$\frac{1}{\tau_A} \sim \frac{n_X}{\hbar k_B T}\left(E_g \frac{a_0^2}{a_B}\right)^2, \tag{D29}$$

where a_0 is the lattice constant. At $T = 4$ K, $a_0 = 3$ Å, $a_B = 1$ nm, $E_B = 0.5$ eV, and the exciton density $n_X = 10^9$ cm^{-2}, this estimate yields $\tau_A \sim 25$ ps.

Let us now take into account the detuning

$$\Delta = E_g' - E_g - E_{B,n} + 2E_B. \tag{D30}$$

Accordingly, we have the sum over $\boldsymbol{K}_{1,2}$ in the following form:

$$\sum_{\boldsymbol{K}_1,\boldsymbol{K}_2} f(K_1) f(K_2)\delta\left[\frac{\hbar^2(K_1^2 + K_2^2 - |\boldsymbol{K}_1 + \boldsymbol{K}_2|^2)}{2M} - \Delta\right] = \frac{n_X^2}{2k_B T}\mathrm{e}^{-|\Delta|/k_B T}. \tag{D31}$$

We see that the difference with the case of zero detuning is the exponent. The Auger recombination rate is given by

$$R_A = R_n \mathrm{e}^{-|\Delta|/k_B T}. \tag{D32}$$

APPENDIX E: TWO-PHOTON ABSORPTION VIA EXCITON STATE

In order to analyze the two-photon absorption via the exciton state, we present a simple three-state model describing the dynamics of the ground state of the crystal $|0\rangle$ (no excitons), $|\mathrm{A}:1s\rangle$ ($\mathrm{A}:1s$ exciton), and excited state $|f\rangle$ (the exciton formed by the electron in the c' band and the hole in the valence band v). Expanding the wavefunction of the system over these states and introducing the decomposition coefficients, respectively, C_0, $C_{\mathrm{A}:1s}$, and C_f, we obtain, from second-order time-dependent perturbation theory,

$$C_0 = 1, \tag{E1a}$$

$$C_{\mathrm{A}:1s} = \frac{V_{A0}}{\hbar\omega - E_{\mathrm{A}:1s} + \mathrm{i}\hbar\Gamma_A}, \tag{E1b}$$

$$C_f = \frac{V_{fA}V_{A0}}{(2\hbar\omega - E_f + \mathrm{i}\hbar\Gamma_f)(\hbar\omega - E_{\mathrm{A}:1s} + \mathrm{i}\hbar\Gamma_A)}. \tag{E1c}$$

Here, ω is the energy of the incident radiation, $E_{\mathrm{A}:1s} = E_g - E_B$ is the excitation energy of the A exciton, E_f is the energy of the exciton in the final state $|f\rangle$, and Γ_A and Γ_f are the dampings of these states. In Eqs. (E1), the matrix elements V_{A0} and V_{Af} are the matrix elements of exciton excitation for the processes $v \to c$ and $c \to c'$, respectively; see below for explicit expressions. In this simplified approach, the steady-state populations of the $\mathrm{A}:1s$ state and of the f state read

$$N_{\mathrm{A}:1s} = |C_{\mathrm{A}:1s}|^2 = \frac{|V_{A0}|^2}{(\hbar\omega - E_A)^2 + \hbar^2\Gamma_A^2}, \tag{E2a}$$

$$N_f = |C_f|^2 = \frac{|V_{fA}|^2}{(2\hbar\omega - E_f)^2 + \hbar^2\Gamma_f^2} \times N_{\mathrm{A}:1s}. \tag{E2b}$$

Note that Eq. (E2a) gives the spectral shape of one-photon absorption in the vicinity of $\mathrm{A}:1s$ exciton resonance, while Eq. (E2b) gives the spectral shape of the two-photon absorption.

It is instructive to estimate the two-photon absorption-induced generation rate of excitons in the excited states. Taking into account that in our model the lifetime of the state $|f\rangle$ reads $\tau_f = 1/(2\Gamma_f)$, the generation rate of the excitons in the $|f\rangle$ state can be

$$R_{TPA} = \frac{N_{\mathrm{A}:1s}}{\tau_{TPA}}, \qquad \frac{1}{\tau_{TPA}} = \frac{2\Gamma_f |V_{fA}|^2}{(2\hbar\omega - E_f)^2 + \hbar^2\Gamma_f^2}. \tag{E3}$$

The calculation shows that the absolute values squared of the matrix elements take the form

$$|V_{A0}|^2 = \left|\frac{e\gamma_3}{E_g}\mathcal{E}_\omega\right|^2 \Phi_{1s}^2(0), \qquad |V_{fA}|^2 = \left|\frac{e\gamma_6}{E_g'}\mathcal{E}_\omega\right|^2. \tag{E4}$$

Here, the normalization area is set to unity. We neglected the difference between $\hbar\omega$ and E_g and E_g' and disregarded the difference of the exciton envelope functions in the intermediate and final states. Note that $\mathcal{E}_\omega$ is the amplitude of the incident electromagnetic field. For crude estimates, we put $\Gamma_f = \Gamma_A \equiv \Gamma$ as well as $\gamma_3 = \gamma_6$ and assume that the double-resonant condition $2\hbar\omega \approx E_f$, $\hbar\omega \approx E_A$ (which overestimates the rate of transition); we obtain

$$\frac{1}{\tau_{TPA}} \sim \Gamma \frac{n_X}{|\Phi_{1s}(0)|^2} \sim \Gamma n_X a_B^2.$$

The estimate (at a reasonable $\Gamma \sim 1$ meV) gives $\tau_{TPA} \sim 100$ ns under the exciton density as the resonant Auger time of $\tau_A \sim 25$ ps estimated in Appendix D 3 [Eq. (D29) and below]. Thus, we may conclude that the direct two-photon absorption is weaker than the Auger-like process.

Note that, strictly speaking, both V_{A0} and V_{fA} are proportional to the amplitude of the incident electric

field $\mathcal{E}_\omega$. Thus, $N_f \propto I^2$. Therefore, in this process, the dependence $I_{\mathrm{up}} \propto I^2$ is expected, in contrast to the experimental observations in Fig. 2(c). The saturation of absorption of the A:1s state resulting in Γ_A being dependent on $n_{\mathrm{A:1}s}$ may somewhat reduce the scaling power of the I_{up} vs I dependence.

[1] K. S. Novoselov, A. Mishchenko, A. Carvalho, and A. H. Castro Neto, *2D Materials and van der Waals Heterostructures*, Science **353**, aac9439 (2016).

[2] A. K. Geim and I. V. Grigorieva, *van der Waals Heterostructures*, Nature (London) **499**, 419 (2013).

[3] K. F. Mak, C. Lee, J. Hone, J. Shan, and T. F. Heinz, *Atomically Thin* MoS_2*: A New Direct-Gap Semiconductor*, Phys. Rev. Lett. **105**, 136805 (2010).

[4] A. Splendiani, L. Sun, Y. Zhang, T. Li, J. Kim, C.-Y. Chim, G. Galli, and F. Wang, *Emerging Photoluminescence in Monolayer* MoS_2, Nano Lett. **10**, 1271 (2010).

[5] Q. H. Wang, K. Kalantar-Zadeh, A. Kis, J. N. Coleman, and M. S. Strano, *Electronics and Optoelectronics of Two-Dimensional Transition Metal Dichalcogenides*, Nat. Nanotechnol. **7**, 699 (2012).

[6] K. F. Mak and J. Shan, *Photonics and Optoelectronics of 2D Semiconductor Transition Metal Dichalcogenides*, Nat. Photonics **10**, 216 (2016).

[7] G. Wang, A. Chernikov, M. M. Glazov, T. F. Heinz, X. Marie, T. Amand, and B. Urbaszek, *Colloquium: Excitons in Atomically Thin Transition metal Dichalcogenides*, Rev. Mod. Phys. **90**, 021001 (2018).

[8] K. He, N. Kumar, L. Zhao, Z. Wang, K. F. Mak, H. Zhao, and J. Shan, *Tightly Bound Excitons in Monolayer* WSe_2, Phys. Rev. Lett. **113**, 026803 (2014).

[9] M. M. Ugeda *et al.*, *Observation of Giant Bandgap Renormalization and Excitonic Effects in a Monolayer Transition Metal Dichalcogenide Semiconductor*, Nat. Mater. **13**, 1091 (2014).

[10] A. Chernikov, T. C. Berkelbach, H. M. Hill, A. Rigosi, Y. Li, O. B. Aslan, D. R. Reichman, M. S. Hybertsen, and T. F. Heinz, *Exciton Binding Energy and Nonhydrogenic Rydberg Series in Monolayer* ws_2, Phys. Rev. Lett. **113**, 076802 (2014).

[11] Z. Ye, T. Cao, K. O'Brien, H. Zhu, X. Yin, Y. Wang, S. G. Louie, and X. Zhang, *Probing Excitonic Dark States in Single-layer Tungsten Disulfide*, Nature (London) **513**, 214 (2014).

[12] D. Y. Qiu, F. H. da Jornada, and S. G. Louie, *Optical Spectrum of* MoS_2*: Many-Body Effects and Diversity of Exciton States*, Phys. Rev. Lett. **111**, 216805 (2013).

[13] A. Ramasubramaniam, *Large Excitonic Effects in Monolayers of Molybdenum and Tungsten Dichalcogenides*, Phys. Rev. B **86**, 115409 (2012).

[14] G. Wang, X. Marie, I. Gerber, T. Amand, D. Lagarde, L. Bouet, M. Vidal, A. Balocchi, and B. Urbaszek, *Giant Enhancement of the Optical Second-Harmonic Emission of* WSe_2 *Monolayers by Laser Excitation at Exciton Resonances*, Phys. Rev. Lett. **114**, 097403 (2015).

[15] C. Jin *et al.*, *Interlayer Electron–Phonon Coupling in* WSe_2/hBN *Heterostructures*, Nat. Phys. **13**, 127 (2017).

[16] M. Manca *et al.*, *Enabling Valley Selective Exciton Scattering in Monolayer* WSe_2 *through Upconversion*, Nat. Commun. **8**, 14927 (2017).

[17] C. M. E. Chow *et al.*, *Unusual Exciton-Phonon Interactions at van der Waals Engineered Interfaces*, Nano Lett. **17**, 1194 (2017).

[18] F. Cadiz *et al.*, *Excitonic Linewidth Approaching the Homogeneous Limit in* MoS_2*-based van der Waals Heterostructures*, Phys. Rev. X **7**, 021026 (2017).

[19] O. A. Ajayi *et al.*, *Approaching the Intrinsic Photoluminescence Linewidth in Transition Metal Dichalcogenide Monolayers*, 2D Mater. **4**, 031011 (2017).

[20] Z. Wang, J. Shan, and K. F. Mak, *Valley- and Spin-Polarized Landau Levels in Monolayer* WSe_2, Nat. Nanotechnol. **12**, 144 (2017).

[21] J. Wierzbowski *et al.*, *Direct Exciton Emission from Atomically Thin Transition Metal Dichalcogenide Heterostructures Near the Lifetime Limit*, Sci. Rep. **7**, 12383 (2017).

[22] S.-Y. Chen, T. Goldstein, J. Tong, T. Taniguchi, K. Watanabe, and J. Yan, *Superior Valley Polarization and Coherence of* 2s *Excitons in Monolayer* WSe_2, Phys. Rev. Lett. **120**, 046402 (2018).

[23] P. Nagler *et al.*, *Zeeman Splitting and Inverted Polarization of Biexciton Emission in Monolayer* WS_2. Phys. Rev. Lett. **121**, 057402 (2018).

[24] S.-Y. Chen, T. Goldstein, T. Taniguchi, K. Watanabe, and J. Yan, *Coulomb-Bound Four- and Five-Particle Valleytronic States in an Atomically-Thin Semiconductor*, arXiv:1802.10247.

[25] W. Seidel, A. Titkov, J. P. André, P. Voisin, and M. Voos, *High-Efficiency Energy Up-Conversion by an "Auger Fountain" at an InP-AlInas Type-II Heterojunction*, Phys. Rev. Lett. **73**, 2356 (1994).

[26] R. Hellmann, A. Euteneuer, S. G. Hense, J. Feldmann, P. Thomas, E. O. Göbel, D. R. Yakovlev, A. Waag, and G. Landwehr, *Low-Temperature Anti-Stokes Luminescence Mediated by Disorder in Semiconductor Quantum-Well Structures*, Phys. Rev. B **51**, 18053 (1995).

[27] E. Poles, D. C. Selmarten, O. I. Mii, and A. J. Nozik, *Anti-Stokes Photoluminescence in Colloidal Semiconductor Quantum Dots*, Appl. Phys. Lett. **75**, 971 (1999).

[28] P. P. Paskov, P. O. Holtz, B. Monemar, J. M. Garcia, W. V. Schoenfeld, and P. M. Petroff, *Photoluminescence Up-Conversion in* InAs/GaAs *Self-Assembled Quantum Dots*, Appl. Phys. Lett. **77**, 812 (2000).

[29] S. L. Chen, J. Stehr, N. Koteeswara Reddy, C. W. Tu, W. M. Chen, and I. A. Buyanova, *Efficient Upconversion of Photoluminescence via Two-Photon Absorption in Bulk and Nanorod ZnO*, Appl. Phys. B **108**, 919 (2012).

[30] A. M. Jones, H. Yu, J. R. Schaibley, J. Yan, D. G. Mandrus, T. Taniguchi, K. Watanabe, H. Dery, W. Yao, and X. Xu, *Excitonic Luminescence Upconversion in a Two-Dimensional Semiconductor*, Nat. Phys. **12**, 323 (2016).

[31] C. Robert *et al.*, *Optical Spectroscopy of Excited Exciton States in* MoS_2 *Monolayers in van der Waals Heterostructures*, Phys. Rev. Mater. **2**, 011001 (2018).

[32] A. Kormanyos, G. Burkard, M. Gmitra, J. Fabian, V. Zólyomi, N. D Drummond, and V. Fal'ko, **k**.**p** *Theory*

for Two-Dimensional Transition Metal Dichalcogenide Semiconductors, 2D Mater. **2**, 022001 (2015).

[33] G. M. Kavoulakis and G. Baym, *Auger Decay of Degenerate and Bose-Condensed Excitons in* Cu_2O, Phys. Rev. B **54**, 16625 (1996).

[34] F. Wang, Y. Wu, M. S. Hybertsen, and T. F. Heinz, *Auger Recombination of Excitons in One-Dimensional Systems*, Phys. Rev. B **73**, 245424 (2006).

[35] S. Dufferwiel *et al.*, *Valley-Addressable Polaritons in Atomically Thin Semiconductors*, Nat. Photonics **11**, 497 (2017).

[36] N. Lundt, A. Maryński, E. Cherotchenko, A. Pant, X. Fan, S. Tongay, G. Sęk, A. V. Kavokin, S. Höfling, and C. Schneider, *Monolayered* $MoSe_2$*: A Candidate for Room Temperature Polaritonics*, 2D Mater. **4**, 015006 (2016).

[37] G. Scuri *et al.*, *Large Excitonic Reflectivity of Monolayer* $MoSe_2$ *Encapsulated in Hexagonal Boron Nitride*, Phys. Rev. Lett. **120**, 037402 (2018).

[38] P. Back, M. Sidler, O. Cotlet, A. Srivastava, N. Takemura, M. Kroner, and A. Imamoğlu, *Giant Paramagnetism-Induced Valley Polarization of Electrons in Charge-Tunable Monolayer* $MoSe_2$, Phys. Rev. Lett. **118**, 237404 (2017).

[39] K. Hao, L. Xu, P. Nagler, A. Singh, K. Tran, C. K. Dass, C. Schüller, T. Korn, X. Li, and G. Moody, *Coherent and Incoherent Coupling Dynamics between Neutral and Charged Excitons in Monolayer* $MoSe_2$, Nano Lett. **16**, 5109 (2016).

[40] T. Taniguchi and K. Watanabe, *Synthesis of High-Purity Boron Nitride Single Crystals under High Pressure by Using Ba-BN Solvent*, J. Cryst. Growth **303**, 525 (2007).

[41] J. S. Ross *et al.*, *Electrical Control of Neutral and Charged Excitons in a Monolayer Semiconductor*, Nat. Commun. **4**, 1474 (2013).

[42] G. Wang, E. Palleau, T. Amand, S. Tongay, X. Marie, and B. Urbaszek, *Polarization and Time-Resolved Photoluminescence Spectroscopy of Excitons in* $MoSe_2$ *Monolayers*, Appl. Phys. Lett. **106**, 112101 (2015).

[43] G. Wang, I. C. Gerber, L. Bouet, D. Lagarde, A. Balocchi, M. Vidal, T. Amand, X. Marie, and B. Urbaszek, *Exciton States in Monolayer* $MoSe_2$*: Impact on Interband Transitions*, 2D Mater. **2**, 045005 (2015).

[44] S. Shree *et al.*, *Exciton-Phonon Coupling in* $MoSe_2$ *Monolayers*, Phys. Rev. B **98**, 035302 (2018).

[45] M. M. Glazov, L. E. Golub, G. Wang, X. Marie, T. Amand, and B. Urbaszek, *Intrinsic Exciton-State Mixing and Nonlinear Optical Properties in Transition Metal Dichalcogenide Monolayers*, Phys. Rev. B **95**, 035311 (2017).

[46] Y.-Q. Bie *et al.*, *A* $MoTe_2$*-based Light-Emitting Diode and Photodetector for Silicon Photonic Integrated Circuits*, Nat. Nanotechnol. **12**, 1124 (2017).

[47] C. Jiang, F. Liu, J. Cuadra, Z. Huang, K. Li, A. Rasmita, A. Srivastava, Z. Liu, and W.-B. Gao, *Zeeman Splitting via Spin-Valley-Layer Coupling in Bilayer* $MoTe_2$, Nat. Commun. **8**, 802 (2017).

[48] T. Goldstein, S.-Y. Chen, J. Tong, D. Xiao, A. Ramasubramaniam, and J. Yan, *Raman Scattering and Anomalous Stokes–Anti-Stokes Ratio in* $MoTe_2$ *Atomic Layers*, Sci. Rep. **6**, 28024 (2016).

[49] S. Song, D. H. Keum, S. Cho, D. Perello, Y. Kim, and Y. H. Lee, *Room Temperature Semiconductor–Metal Transition of* $MoTe_2$ *Thin Films Engineered by Strain*, Nano Lett. **16**, 188 (2016).

[50] Y. Li, K.-A. N. Duerloo, K. Wauson, and E. J. Reed, *Structural Semiconductor-to-Semimetal Phase Transition in Two-Dimensional Materials Induced by Electrostatic Gating*, Nat. Commun. **7**, 10671 (2016).

[51] Y. Wang *et al.*, *Structural Phase Transition in Monolayer* $MoTe_2$ *Driven by Electrostatic Doping*, Nature (London) **550**, 487 (2017).

[52] D. Rhodes *et al.*, *Engineering the Structural and Electronic Phases of* $MoTe_2$ *through W Substitution*, Nano Lett. **17**, 1616 (2017).

[53] C. Ruppert, O. B. Aslan, and T. F. Heinz, *Optical Properties and Band Gap of Single- and Few-Layer* $MoTe_2$ *Crystals*, Nano Lett. **14**, 6231 (2014).

[54] I. G. Lezama, A. Arora, A. Ubaldini, C. Barreteau, E. Giannini, M. Potemski, and A. F. Morpurgo, *Indirect-to-Direct Band Gap Crossover in Few-Layer* $MoTe_2$, Nano Lett. **15**, 2336 (2015).

[55] C. Robert *et al.*, *Excitonic Properties of Semiconducting Monolayer and Bilayer* $MoTe_2$, Phys. Rev. B **94**, 155425 (2016).

[56] G. Froehlicher, E. Lorchat, and S. Berciaud, *Direct Versus Indirect Band Gap Emission and Exciton-Exciton Annihilation in Atomically Thin Molybdenum Ditelluride* $(MoTe_2)$, Phys. Rev. B **94**, 085429 (2016).

[57] N. S. Rytova, *Screened Potential of a Point Charge in a Thin Film*, Proc. MSU, Phys., Astron. **3**, 30 (1967).

[58] L. V. Keldysh, *Coulomb Interaction in Thin Semiconductor and Semimetal Films*, Sov. J. Exp. Theor. Phys. Lett. **29**, 658 (1979).

[59] J. Yang, T. Lü, Y. W. Myint, J. Pei, D. Macdonald, J.-C. Zheng, and Y. Lu, *Robust Excitons and Trions in Monolayer* $MoTe_2$, ACS Nano **9**, 6603 (2015).

[60] D. van Tuan, M. Yang, and H. Dery, *The Coulomb Interaction in Monolayer Transition-Metal Dichalcogenides*, arXiv:1801.00477.

[61] A. V. Stier, N. P. Wilson, K. A. Velizhanin, J. Kono, X. Xu, and S. A. Crooker, *Magnetooptics of Exciton Rydberg States in a Monolayer Semiconductor*, Phys. Rev. Lett. **120**, 057405 (2018).

[62] A. V. Stier, N. P. Wilson, G. Clark, X. Xu, and S. A. Crooker, *Probing the Influence of Dielectric Environment on Excitons in Monolayer* WSe_2*: Insight from High Magnetic Fields*, Nano Lett. **16**, 7054 (2016).

[63] M. Trushin, M. O. Goerbig, and W. Belzig, *Optical Absorption by Dirac Excitons in Single-Layer Transition-Metal Dichalcogenides*, Phys. Rev. B **94**, 041301 (2016).

[64] S. Larentis, H. C. P. Movva, B. Fallahazad, K. Kim, A. Behroozi, T. Taniguchi, K. Watanabe, S. K. Banerjee, and E. Tutuc, *Large Effective Mass and Interaction-Enhanced Zeeman Splitting of k-Valley Electrons in* $MoSe_2$, Phys. Rev. B **97**, 201407 (2018).

[65] H. C. P. Movva, B. Fallahazad, K. Kim, S. Larentis, T. Taniguchi, K. Watanabe, S. K. Banerjee, and E. Tutuc, *Density-Dependent Quantum Hall States and Zeeman Splitting in Monolayer and Bilayer* WSe_2, Phys. Rev. Lett. **118**, 247701 (2017).

[66] R. Pisoni *et al.*, *Interactions and Magnetotransport through Spin-Valley Coupled Landau Levels in Monolayer* MoS_2, arXiv:1806.06402.

[67] S. Mouri, Y. Miyauchi, M. Toh, W. Zhao, G. Eda, and K. Matsuda, *Nonlinear Photoluminescence in Atomically Thin Layered* WSe_2 *Arising from Diffusion-Assisted Exciton-Exciton Annihilation*, Phys. Rev. B **90**, 155449 (2014).

[68] N. Kumar, Q. Cui, F. Ceballos, D. He, Y. Wang, and H. Zhao, *Exciton-Exciton Annihilation in* $MoSe_2$ *Monolayers*, Phys. Rev. B **89**, 125427 (2014).

[69] V. N. Abakumov, V. I. Perel, and I. N. Yassievich, *Nonradiative Recombination in Semiconductors* (North Holland, Amsterdam, 1991).

[70] A. S. Polkovnikov and G. G. Zegrya, *Auger recombination in semiconductor quantum wells*, Phys. Rev. B **58**, 4039 (1998).

[71] D. V. Rybkovskiy, I. C. Gerber, and M. V. Durnev, *Atomically Inspired k.p Approach and Valley Zeeman Effect in Transition Metal Dichalcogenide Monolayers*, Phys. Rev. B **95**, 155406 (2017).

[72] D. Sun, Y. Rao, G. A. Reider, G. Chen, Y. You, L. Brézin, A. R. Harutyunyan, and T. F. Heinz, *Observation of Rapid Exciton-Exciton Annihilation in Monolayer Molybdenum Disulfide*, Nano Lett. **14**, 5625 (2014).

[73] Y. Yu, Y. Yu, C. Xu, A. Barrette, K. Gundogdu, and L. Cao, *Fundamental Limits of Exciton-Exciton Annihilation for Light Emission in Transition Metal Dichalcogenide Monolayers*, Phys. Rev. B **93**, 201111 (2016).

[74] L. Yuan, T. Wang, T. Zhu, M. Zhou, and L. Huang, *Exciton Dynamics, Transport, and Annihilation in Atomically Thin Two-Dimensional Semiconductors*, J. Phys. Chem. Lett. **8**, 3371 (2017).

[75] Y. Hoshi, T. Kuroda, M. Okada, R. Moriya, S. Masubuchi, K. Watanabe, T. Taniguchi, R. Kitaura, and T. Machida, *Suppression of Exciton-Exciton Annihilation in Tungsten Disulfide Monolayers Encapsulated by Hexagonal Boron Nitrides*, Phys. Rev. B **95**, 241403 (2017).

[76] C. Ciuti, V. Savona, C. Piermarocchi, A. Quattropani, and P. Schwendimann, *Role of the Exchange of Carriers in Elastic Exciton-Exciton Scattering in Quantum Wells*, Phys. Rev. B **58**, 7926 (1998).

[77] V. Shahnazaryan, I. Iorsh, I. A. Shelykh, and O. Kyriienko, *Exciton-Exciton Interaction in Transition-Metal Dichalcogenide Monolayers*, Phys. Rev. B **96**, 115409 (2017).

[78] M. Selig, G. Berghäuser, A. Raja, P. Nagler, C. Schüller, T. F. Heinz, T. Korn, A. Chernikov, E. Malic, and A. Knorr, *Excitonic Linewidth and Coherence Lifetime in Monolayer Transition Metal Dichalcogenides*, Nat. Commun. **7**, 13279 (2016).

[79] M. Selig *et al.*, *Dark and Bright Exciton Formation, Thermalization, and Photoluminescence in Monolayer Transition Metal Dichalcogenides*, arXiv:1703.03317.

[80] D. Christiansen *et al.*, *Phonon Sidebands in Monolayer Transition Metal Dichalcogenides*, Phys. Rev. Lett. **119**, 187402 (2017).

[81] A. O. Slobodeniuk and D. M. Basko, *Exciton-Phonon Relaxation Bottleneck and Radiative Decay of Thermal Exciton Reservoir in Two-Dimensional Materials*, Phys. Rev. B **94**, 205423 (2016).

[82] C. Robert *et al.*, *Exciton Radiative Lifetime in Transition Metal Dichalcogenide Monolayers*, Phys. Rev. B **93**, 205423 (2016).

[83] Y. Li, J. Zhang, D. Huang, H. Sun, F. Fan, J. Feng, Z. Wang, and C. Z. Ning, *Room-Temperature Continuous-Wave Lasing from Monolayer Molybdenum Ditelluride Integrated with a Silicon Nanobeam Cavity*, Nat. Nanotechnol. **12**, 987 (2017).

[84] S. Wu *et al.*, *Monolayer Semiconductor Nanocavity Lasers with Ultralow Thresholds*, Nature (London) **520**, 69 (2015).

[85] A. Chernikov, C. Ruppert, H. M. Hill, A. F. Rigosi, and T. F. Heinz, *Population Inversion and Giant Bandgap Renormalization in Atomically Thin ws 2 Layers*, Nat. Photonics **9**, 466 (2015).

[86] H. Guo, T. Yang, M. Yamamoto, L. Zhou, R. Ishikawa, K. Ueno, K. Tsukagoshi, Z. Zhang, M. S. Dresselhaus, and R. Saito, *Double Resonance Raman Modes in Monolayer and Few-Layer* $MoTe_2$, Phys. Rev. B **91**, 205415 (2015).

[87] P. Tonndorf *et al.*, *Photoluminescence Emission and Raman Response of Monolayer* MoS_2, $MoSe_2$, *and* WSe_2, Opt. Express **21**, 4908 (2013).

[88] B. R. Carvalho, L. M. Malard, J. M. Alves, C. Fantini, and M. A. Pimenta, *Symmetry-Dependent Exciton-Phonon Coupling in 2D and Bulk* MoS_2 *Observed by Resonance Raman Scattering*, Phys. Rev. Lett. **114**, 136403 (2015).

[89] G. Wang, M. M. Glazov, C. Robert, T. Amand, X. Marie, and B. Urbaszek, *Double Resonant Raman Scattering and Valley Coherence Generation in Monolayer WSe*, Phys. Rev. Lett. **115**, 117401 (2015).

[90] M. R. Molas, K. Nogajewski, M. Potemski, and A. Babiński, *Raman Scattering Excitation Spectroscopy of Monolayer ws 2*, Sci. Rep. **7**, 5036 (2017).

[91] P. Soubelet, A. E. Bruchhausen, A. Fainstein, K. Nogajewski, and C. Faugeras, *Resonance Effects in the Raman Scattering of Monolayer and Few-Layer* $MoSe_2$, Phys. Rev. B **93**, 155407 (2016).

[92] M. M. Glazov, T. Amand, X. Marie, D. Lagarde, L. Bouet, and B. Urbaszek, *Exciton Fine Structure and Spin Decoherence in Monolayers of Transition Metal Dichalcogenides*, Phys. Rev. B **89**, 201302 (2014).

[93] P. Cudazzo, I. V. Tokatly, and A. Rubio, *Dielectric Screening in Two-Dimensional Insulators: Implications for Excitonic and Impurity States in Graphane*, Phys. Rev. B **84**, 085406 (2011).

[94] G. L. Bir and G. E. Pikus, *Symmetry and Strain-Induced Effects in Semiconductors* (Wiley/Halsted Press, New York, Toronto, 1974).

[95] C. Y. -P. Chao and S. L. Chuang, *Analytical and Numerical Solutions for a Two-Dimensional Exciton in Momentum Space*, Phys. Rev. B **43**, 6530 (1991).